Joint Polar Satellite System (JPSS) Ground Project

Joint Polar Satellite System (JPSS) Advanced Technology Microwave Sounder (ATMS) SDR Calibration Algorithm Theoretical Basis Document (ATBD)

For Public Release

National Oceanic and Atmospheric Administration

Center for Satellite Applications and Research
College Park, Maryland

This page intentionally left blank.

Joint Polar Satellite System
Advanced Technology Microwave Sounder (ATMS)
SDR Radiometric Calibration
Algorithm Theoretical Basis Document (ATBD)

JPSS Electronic Signature Page

Prepared By:

JPSS ATMS SDR Science Team
(Electronic Approvals available online at http://www.star.nesdis.noaa.gov/jpss/ATBD.php)
Point of Contact/Custodian: Quanhua Liu (Quanhua.Liu@noaa.gov)

Approved By:

JPSS Ground System

Lihang Zhou (Lihang.Zhou@noaa.gov)
JPSS Enterprise Product Management Lead
Algorithm Engineering Review Board (AERB) Chair
JPSS Ground Project

Doug Howard (Douglas.Howard@noaa.gov)
JPSS-STAR (JSTAR) Lead
Chief, Satellite Meteorology and Climatology Division
NOAA Center for Satellite Applications and Research (STAR)

Changyong Cao (Changyong.Cao@noaa.gov)
JPSS-STAR SDR Team Lead
Chief, Satellite Calibration & Data Assimilation Branch
NOAA Center for Satellite Applications and Research (STAR)

Center for Satellite Applications and Research
College Park, Maryland

Disclaimer: The scientific results and conclusions, as well as any views or opinions expressed herein, are those of the author(s) and do not necessarily reflect those of NOAA or the Department of Commerce.

This page intentionally left blank.

Change History Log

Center for Satellite Applications and Research National Center for Weather and Climate Prediction College Park, Maryland			
Revision/Change Record		For Document No.	**D0001-M01-S01-001_JPSS_ATBD_ATMS_SDR**

Revision	Document Date	Revision/Change Description	Pages Affected
Baseline	27 Jan 2010	Public Released version	All
Rev-A Version 1	18 Dec 2013	Modified baseline version with the following additions from Suomi NPP cal/val: TDR to SDR conversion theory for scan angle bias correction, resampling SDR theory, striping analysis and lunar intrusion correction.	All
Rev-B Version 1	14 Jun 2022	Modified to reflect the change from temperature to radiance calibration approach, addition of reflector emission correction and lunar intrusion correction, and removal of Cross-Track Infrared and Microwave Sounder Suite (CrIMSS) and product remapping requirements. Added the operational noise equivalent differential temperature algorithm, as well as an improved recommended algorithm.	All

This page intentionally left blank.

Table of Contents

Table of Figures

Table of Tables

Acronyms

ADC	Analog-to-Digital Converter
AIRS	Atmospheric Infrared Sounder
AMSU	Advanced Microwave Sounding Unit
ATBD	Algorithm Theoretical Basis Document
ATMS	Advanced Technology Microwave Sounder
CCA	Circuit Card Assembly
DN	Data Number
DPLX	Diplexer
EDR	Environmental Data Record
EOS	Earth Observing System
EU	Engineering Unit
EUMETSAT	European Organization for the Exploitation of Meteorological Satellites
GEO	GEOlocation
HAMSR	High Altitude MMIC Sounding Radiometer
HIRS	High resolution Infrared Radiation Sounder
HKPG	HouseKeePinG
IF	Intermediate Frequency
IMAS	Integrated Multispectral Atmospheric Sounder
IMF	Instantaneous Measurement Frequency
IDPS	Interface Data Processing Segment
IR	Infrared
LO	Local Oscillator
LNR	Low-Noise Receiver
MHS	Microwave Humidity Sounder
MMIC	Monolithic Microwave Integrated Circuit
MSU	Microwave Sounding Unit
MUX	MUltipleXer
MW	MicroWave
MXR	MiXeR
NASA	National Aeronautics and Space Administration
NEDT	Noise-Equivalent Differential Temperature
NGES	Northrop Grumman Electronic Systems
NOAA	National Oceanic and Atmospheric Administration
NPOESS	National Polar-orbiting Operational Environmental Satellite System
NPP	NPOESS Preparatory Project
PLLO	Phase Locked Local Oscillator
POES	Polar-orbiting Operational Environmental Satellite
PRT	Platinum Resistance Thermometer
QA	Quality Assessment
QC	Quality Control
RDR	Raw Data Record
RF	Radio Frequency
RFE	Radiometer Front End
SAW	Surface Acoustic Wave

SDR	**S**ensor **D**ata **R**ecord
TDR	**T**emperature **D**ata **R**ecord

1. Introduction

This Advanced Technology Microwave Sounder (ATMS) Algorithm Theoretical Basis Document (ATBD) describes the theoretical basis, and to a limited extent the implementation, of algorithms used for converting ATMS instrument raw data numbers (DN) or engineering units (EU) contained in Raw Data Record (RDR) files into calibrated brightness temperatures contained in Temperature Data Record (TDR) and Sensor Data Record (SDR) product files. The RDRs are raw and minimally processed instrument telemetry, and are the input to TDR/SDR processing. The SDR product is the output from SDR processing, and serves as the input to Environmental Data Record (EDR) product generation, where the ATMS calibrated brightness temperatures are converted to geophysical parameters through a "retrieval" process. The SDR or TDR and Geolocation (GEO), are also the inputs to the direct radiance assimilation system that supports weather forecasting at numerical weather prediction centers.

The algorithms described in this document have a similar foundation to those developed by the National Oceanic and Atmospheric Administration (NOAA) for the Advanced Microwave Sounding Unit-A (AMSU-A) and Microwave Humidity Sounder (MHS) instruments (Mo, 2002 and Mo and Jarva, 2004). These microwave radiometers have been flown since 1998 on the NOAA Polar-orbiting Operational Environmental Satellite (POES), Earth Observing System (EOS) Aqua, and European Organization for the Exploitation of Meteorological Satellites (EUMETSAT) MetOp satellite platforms. Although the basic functionalities and principles of operation of these instruments are quite similar to ATMS, there are minor differences between the respective algorithmic approaches.

Details of ATMS ATBD Rev. A Version 1 were based on a preliminary software algorithm developed by the ATMS contractor, Northrop Grumman Electronic Systems (NGES) (changed to Northrop Grumman Space System (NGSS) in 2016). The documentation associated with this preliminary algorithm was delivered by NGSS in mid-2004, and released publicly as the ATMS ATBD baseline version on 27 January 2010. The current document reflects algorithm changes since the baseline version to accommodate ATMS post-launch algorithm development and requirements changes. For example, the calibration is now performed in radiance units before converting to brightness temperature near the end of processing, a reflector emission correction has been added, and the Cross-Track Infrared and Microwave Sounder Suite (CrIMSS) and product remapping requirements have been removed. A table of Interface Data Processing Segment (IDPS) operational releases associated with ATMS SDR algorithm changes can be found in Table 1. Note that new ATBD revisions have not been distributed at the same time as these IDPS algorithm releases, but going forward effort will be made to synchronize them.

Table **1.** The IDPS operational release date, event description and applicable instrument unit(s) associated with the ATMS SDR algorithm and processing coefficient table (PCT) changes.

Date	Event	S-NPP	NOAA-20	JPSS-2	JPSS-3	JPSS-4
14 Nov 2013	Antenna pattern correction coefficients update in PCT	Yes	N/A	N/A	N/A	N/A
18 Mar 2014	Warm count & spaceview count max/min limits update in PCT	Yes	N/A	N/A	N/A	N/A
8 Mar 2017	1. Full radiance calibration algorithm update in IDPS and	1. Yes 2. Yes	N/A	N/A	N/A	N/A

	2. Nonlinearity correction coefficients update in PCT					
8 Dec 2017	Antenna pattern correction coefficients update in PCT	N/A	Yes	N/A	N/A	N/A
30 Apr 2018	Antenna pattern correction coefficients and data quality control limits update in PCT	N/A	Yes	N/A	N/A	N/A
15 Oct 2019	1. Reflector emission correction algorithm update in IDPS 2. Antenna pattern correction coefficients update in PCT 3. PCT update on reflector emission correction coefficients	1. Yes 2. Yes 3. N/A	1. Yes 2. N/A 3. Yes	N/A	N/A	N/A
4 Feb 2021	Lunar intrusion correction algorithm update in IDPS and lunar intrusion correction coefficients update in PCT	Yes	Yes	N/A	N/A	N/A

Although it is intended that this ATBD be readable as a standalone document, it is recommended that the reader references the related instrument and system description documents available from the following: The 2013 special issue on Suomi-NPP Satellite Calibration, Validation and Applications published by the Journal of Geophysical Research Atmosphere; and more recent literature reflecting the theory and results related to ATMS algorithm changes (Kim et. al., 2013 and Weng et al., 2013). In this ATBD, there is a brief description of the instrument itself, and an explanation of references to devices, procedures, and tables used by the TDR/SDR algorithms. The present document contains some as-built and on-orbit performance characteristics where needed for reference.

The document also describes the functions performed by the ground processing system. However, note that nothing is implied in this ATBD about the architecture or the implementation of the system. The detailed information about how the theoretic calibration algorithm is implemented in the operational ground processing system can be found in the JPSS Operational Algorithm Description (OAD) document [*NASA*, 2017]

2. Historical Perspective

The ATMS is designed to meet the weather requirements for NOAA and climate research objectives of the National Aeronautics and Space Administration (NASA). The first version of ATMS is flown on the Suomi-National Polar-Orbiting Partnership (SNPP) mission on 28 October 2011 and subsequently on a series of Joint Polar Satellite System (JPSS) missions. Since continuity of sounding capabilities is an important requirement for operational microwave radiometers, it is useful to know the history of predecessor microwave radiometers to ATMS. This history is described briefly below.

The earliest operational microwave sounding instrument was the Microwave Sounding Unit (MSU). The MSU radiometers that operated on NOAA POES platforms were the principal sources of satellite temperature profiles from late 1978 to the early 2000's. The MSU instruments were cross-track scanners that made measurements of microwave radiance in four channels ranging from 50.3 to 57.95 GHz on the lower frequency shoulder of the oxygen absorption band. These four channels measured the atmospheric temperature in four thick layers spanning the surface through the stratosphere. There were 9 MSU models in total. The last MSU instrument flew on NOAA-14, and ceased reliable operation in 2007.

A follow-on instrument to the MSU is the AMSU, and the first AMSU on NOAA-15 began operation in 1998. The AMSU instruments are composed of 2 sub units, AMSU-A and AMSU-B. AMSU-A is a 15-channel temperature sounder similar to MSU, and AMSU-B is a 5-channel humidity sounder. Eleven of the 15 AMSU-A channels - Channels 4 through 14 - are located in the 60 GHz oxygen absorption complex, and thus are most closely related to atmospheric temperature at various heights above the surface. The increased number of channels relative to MSU means that AMSU-A samples the temperature of the atmosphere in a larger number of layers. The AMSU measurement footprints are also smaller than those for MSU, leading to higher spatial resolution. The linkage between AMSU-A and MSU lies between AMSU-A Channels 3, 5, 7, and 9 and MSU Channels 1, 2, 3, and 4, respectively. The AMSU-B instrument has channels from 89 to 183 GHz, and is used to study profiles of atmospheric water vapor, and provide improved input data to the cloud-clearing algorithms in infrared/microwave (IR/MW) sounder suites. This instrument was replaced by MHS in May 2005 on NOAA-18 and after, and has two channels that differ from AMSU-B. The MHS hardware is similar, not exactly the same as AMSU-B. It has channels at 157.0 GHz and 190.311 GHz that replace the AMSU-B 150.0±0.9 GHz and 183.31±0.7 GHz channels, respectively. Also, the 183.31±0.1 GHz and 183.31±0.3 GHz channels of AMSU-B were converted from vertical to horizontal polarization sensitivity in the switch to MHS.

During the mid-1990's, while the Atmospheric Infrared Sounder (AIRS) was being built, an effort was made by NASA to transfer the AIRS technology to NOAA operations, with the goal of providing an AIRS follow-on instrument for the National Polar-orbiting Operational Environmental Satellite System (NPOESS, now JPSS) missions. A technology development effort was launched, with a primarily focus on reducing the mass, size, and power consumption of the microwave component of the sounding suite this time. The proposed system was called the Integrated Multispectral Atmospheric Sounder (IMAS) – a single combined infrared and microwave instrument that was intended to fly as a demonstration on the NASA New Millennium Program's EO-3 mission. The effort was terminated in mid-1998 largely due to cost constraints, but many of the IMAS microwave specifications were later adopted for the ATMS instrument.

It was initially the intention to use the 118-GHz oxygen absorption line for temperature sounding in the IMAS system, instead of the 50-60 GHz band used by AMSU. This would make it possible to shrink the aperture by a factor of more than two (and therefore also the overall mass and size) while maintaining spatial resolution and other performance measures. A field of view (FOV) of the same size as the IR sounder (i.e. 1.1°) was highly desired, and the IMAS/MW component was therefore designed to have this beam width for all sounding channels - i.e., in the 118-GHz band for temperature sounding and in the 183-GHz band for water vapor sounding. Later, it was realized that even the most transparent 118-GHz channels may not be able to penetrate the atmosphere to the Earth surface under very humid and cloudy conditions (e.g., in the tropics). In addition, scattering signatures for 118-GHz bands are stronger than that for 50-GHz, which can complicate applications. The 50-GHz band then needed to be restored to provide backup capabilities for such situations. A compromise was made to use the same aperture size at 50 GHz as at 118 GHz, and a 2.5° beam width. The IMAS team also determined that the microwave instrument should have the same spectral channels as AMSU for "science continuity" and that a few additional channels were desirable. As a result, two new channels were suggested to be added in the 183-GHz band, and one new window channel be added in between 50 GHz and 60 GHz. In addition, the 150-GHz (157.0-GHz) quasi-window channel used in AMSU-B(MHS) was replaced with one at 166 GHz, which can be operated as part of an advanced-technology of the 183-GHz receiver (thus saving one receiver chain). These were considerations provided by the AIRS team. Most of these specifications and characteristics are now part of the ATMS specifications except for the 118-GHz band, which was eliminated early in the program due to cost constraints, and the 2.5° beam width which was improved to 2.2°.

The most significant advancement under IMAS was the development of monolithic microwave integrated circuit (MMIC) technology at sounding frequencies - i.e. at 50, 118 and 183 GHz - which allows for sensitive and compact receivers and spectrometers. Such a technology was previously only available at considerably lower frequencies. Sample receivers and compact solid-state filter banks were developed for the two lower frequency bands, and low-noise amplifiers (i.e. precursors to full receivers) were developed for the 183-GHz band. After the termination of IMAS these technological items were incorporated into an aircraft-based microwave sounder called the High Altitude MMIC Sounding Radiometer (HAMSR), developed under the NASA Instrument Incubator Program. HAMSR may be viewed as an ATMS precursor as a prototype of ATMS in many respects. HAMSR uses a dual aperture with two reflectors operating on a common axis, which was adopted for ATMS. HAMSR has been successfully operated on the NASA ER-2 high altitude aircraft since 2001. In summary, ATMS has heritage primarily from AMSU, the IMAS design, and the HAMSR.

3. Instrument Description

In this section we give a brief description of the ATMS instrument. ATMS instrument layout is illustrated in Figure 1. ATMS is a 22-channel microwave sounder providing both temperature soundings between the surface and the upper stratosphere (i.e. to about 1 mb, at an altitude of about 45 km) and humidity soundings between the surface and the upper troposphere (i.e. to about 200 mb, at an altitude of about 15 km). Like AMSU, it is a cross-track scanner. There are two receiving apertures — one serving 15 channels below 60 GHz with a beam width of 2.2° except for the lowest two channel frequencies, and the other serving seven channels above 60 GHz with a beam width of 1.1° except for the lowest channel frequency as listed in Table 2.
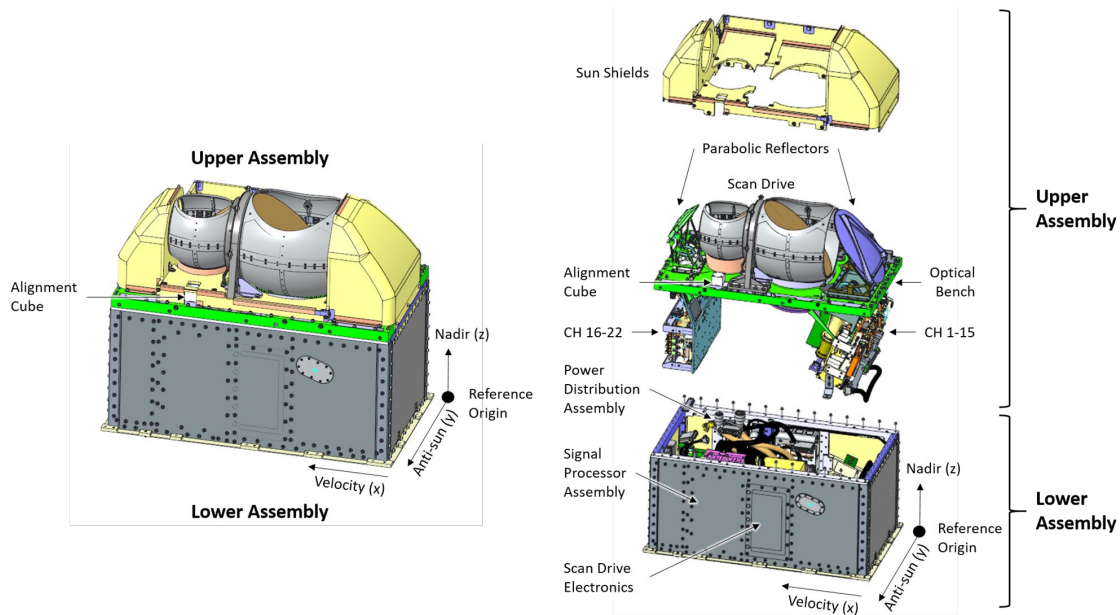
Figure 1. ATMS instrument layout

The antennas consist of plane reflectors mounted on a scan axis at a 45° tilting angle, so that radiation from a direction perpendicular to the scan axis is reflected into a direction parallel to the scan axis - i.e. a 90° reflection. With the scan axis being oriented in the along-track direction, this results in a cross-track scanning pattern. The reflected radiation is then focused by a stationary parabolic reflector onto a dichroic plate, and finally either reflected to or passed to a feedhorn. In other words, radiation from a direction within the scan plane, which depends on the angle of rotation of the reflector, is reflected and focused onto the receiver apertures, which are conical feedhorns. A schematic illustration of one-of-two ATMS antenna and radio frequency (RF) feed subsystems is provided in Figure 2.
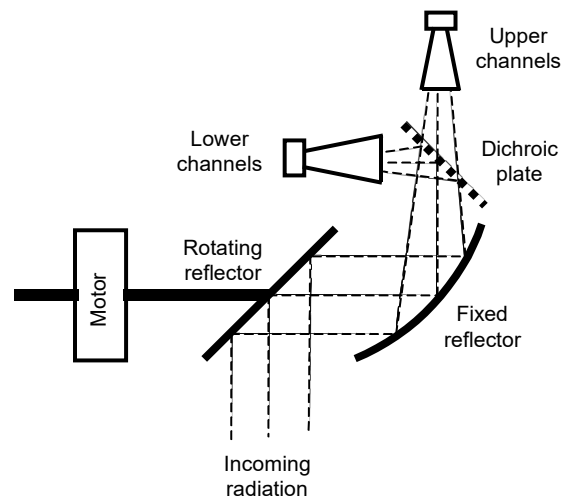
Figure 2. Schematic of one of two ATMS antenna and RF feed subsystems.

The ATMS antenna system is designed such that a slightly diverging conical pencil "beam" is formed with a half-power width (also called the 3-dB width) of being either 1.1°, 2.2°, or 5.2°, with a possible variation being within ±10% from channel to channel. The antenna response pattern typically consists of a prominent Gaussian-shaped half-power cone at the center, but also receives a significant portion of its energy outside of this cone. Approximately 95-97% of the energy is received within the so-called main beam, which is defined as 2.5 times the half-power beam width, i.e., the ATMS "main beam" is either 2.75°, 5.5° or 13° wide. A significant amount of energy (i.e. up to 5%) is thus received from outside the main beam. Figure 3 shows a typical antenna pattern. The pattern in the vicinity of the main beam is called the near sidelobes, while that further away is called the far sidelobes. The far sidelobes can contribute significantly to the measurement errors.
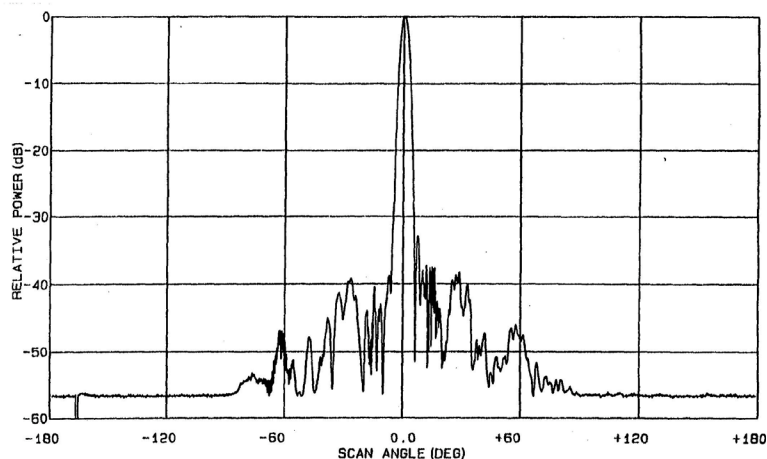
Figure 3. Typical microwave antenna pattern

For the K-band (channel 1), Ka-band (channel 2) and G-band (channels 17-22), the feedhorn is followed by a diplexer (DPLX) that splits the RF energy into two parallel signal paths that proceed to their respective receivers, which is in most cases a heterodyne system. The G-band signal is further converted by a mixer (MXR), while the signals from all three bands are separated into channels with filters, and detected. Figure 4 shows a diagram of the ATMS system. Discussions on various signal paths that lead to the individual spectral channel outputs are provided below.
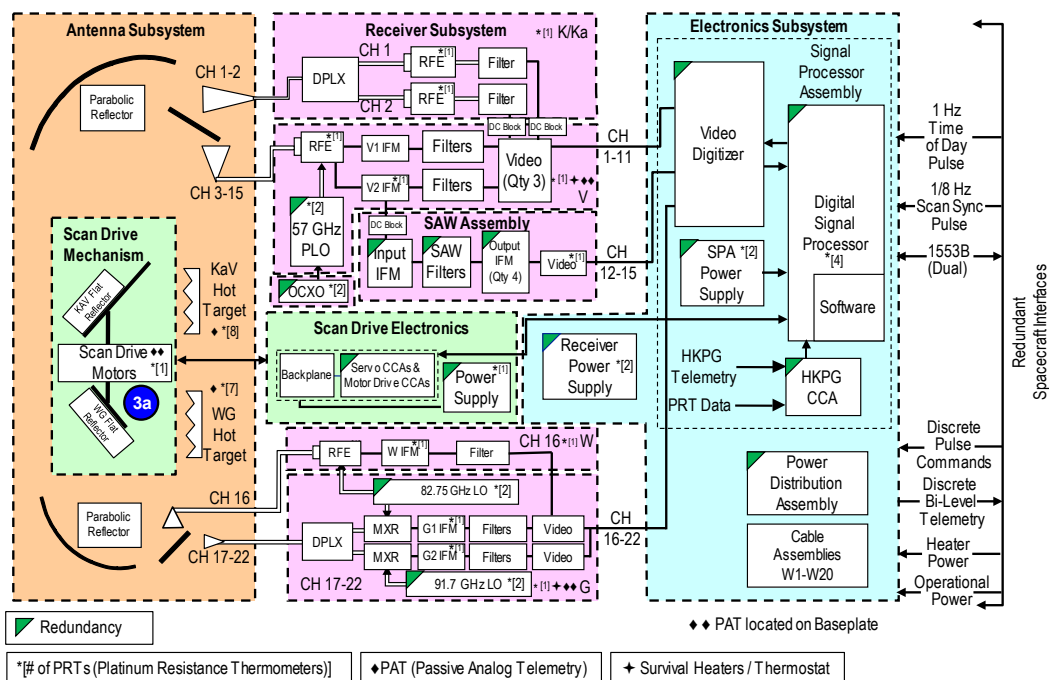
Figure 4. ATMS block diagram

The large reflector is used for the 15 lowest-frequency channels, which are sometimes referred to as the KAV-aperture, since it covers K-band, Ka-band and V-band (channels 3-15). The dichroic plate, which reflects frequencies below a certain value and transmits those above, splits the RF energy into a low and high frequency paths. The output of the low frequency feedhorn enters a diplexer, which in turn splits the now somewhat band-limited RF energy into two parallel paths. Each path is fed into an amplified receiver chain, followed by a bandpass filter centered either at 23.8 GHz (channel 1) or at 31.4 GHz (channel 2). These are the only non-heterodyne receivers in the ATMS system.

The output of the higher frequency feedhorn is mixed with a common phase-locked local oscillator (PLO) operating at 57.290344 GHz into an amplified, and bandpass filtered, heterodyne receiver with two down-converter/mixer chains. The LO is a highly stable and temperature-controlled crystal referenced phase locked oscillator. One path is lowpass filtered, resulting in a single-sideband intermediate frequency (IF) band located at 1.6 – 7.1 GHz below the LO frequency. This band is in turn passed through a set of signal splitters/multiplexers and bandpass filters that select channels 3-9. The other path is bandpass filtered, resulting in a double-sideband IF band located at 10 – 400 MHz away from the LO frequency. Two channels (10 and 11) are formed with conventional bandpass filters similar to those used for channels 3-9, while the remaining channels (12-15) are formed with a standing acoustic wave (SAW) filter assembly. Note that the SAW assembly is implemented as a set of four pairs of filters, each positioned symmetrically with respect to an IF frequency of 322.2 MHz. The outputs of each filter pair are combined and amplified. Channels 12-15 are therefore in effect quadruple-sideband channels.

A smaller aperture is used for the seven highest frequency channels and is sometimes referred to as the WG-aperture, since it covers W-band (channel 16) and G-band (channels 17-22). Here the lower frequency path - i.e., the signal reflected from the dichroic plate - enters a single feedhorn and an amplified highpass filtered heterodyne receiver chain, where the mixer uses an LO operating at 82.75 GHz, producing a single upper sideband IF signal that is finally put through a 4450-6450 MHz bandpass filter for channel 16 (which results in a channel located at 87.2-89.2 GHz). The high frequency path, i.e., the transmitted signal through the dichroic plate, enters a smaller feedhorn followed by a diplexer that splits the signal into two paths. One path goes to a second harmonic mixer that uses the same LO as the channel 16 receiver. The resulting double sideband IF signal is put through a 350-1500 MHz bandpass filter for channel 17, which is then located at 164-167 GHz with a gap between 165.15-165.85 GHz. The second path goes to a second harmonic mixer, which uses an LO operating at 91.655 GHz. The double sideband IF is passed through a set of filters that produce channels 18-22. These channels are therefore centered at $183.31 \text{ GHz} \pm \Delta f$, where Δf is 7, 4.5, 3, 1.8 or 1 GHz, with their bandpass width varying from channel to channel.

Table 2 summarizes the JPSS performance specifications of all 22 channels, including radiometric sensitivity, which is usually called noise equivalent differential temperature (NEDT). It lists three frequency specifications: nominal center frequency, center frequency stability (i.e., the allowed maximum deviation from the nominal center frequency value), and bandwidth (specified and designed). All are given in MHz. Note that the number of pass-bands per channel, listed in the "Center Frequency" column of the table, is the maximum allowed. Fewer pass-bands may be used in the design, provided the Temperature Sensitivity requirements are met. For example, Channel 18 lists two pass-bands centered at $(183.31 + 7) = 190.31$ GHz and $(183.31-7) = 176.31$ GHz. The channel may be implemented using only one of these passbands, provided the temperature sensitivity value of no greater than 0.8 K is achieved. The designed bandwidth notation is "N$\times\Delta$f",

where N is the number of sub-bands used for a channel and Δf is the width of each sub-band. For example, 2x270 means a double-band channel with each of the two bands being 270 MHz wide.

Requirements for beamwidth and calibration accuracy are also listed in Table 2. A single linear polarization is measured for each channel. The nominal polarization direction at the nadir scan position is also listed in the table. Each build's real measured values can also be found in the measured spectral response function (SRF) data post in NOAA STAR JPSS web site (https://www.star.nesdis.noaa.gov/jpss/ATMS.php).

Table 2. JPSS ATMS spectrometric and radiometric specifications.

Ch	RF path			Center frequency [MHz]		Bandwidth [MHz]		NEDT [K]	Pol	Beamwidth [°]	Accuracy [K]
	Ant	Feed	Rcvr	Value	Stab	Req	Design	Req		Req	Req
1	A	1	a	23800	<10	<270	1x270	0.7	QV	5.2	1.0
2	A	1	b	31400	<10	<180	1x180	0.8	QV	5.2	1.0
3	A	2	c	50300	<10	<180	1x180	0.9	QH	2.2	0.75
4	A	2	c	51760	< 5	<400	1x400	0.7	QH	2.2	0.75
5	A	2	c	52800	< 5	<400	1x400	0.7	QH	2.2	0.75
6	A	2	c	53596±115	< 5	170	2x170	0.7	QH	2.2	0.75
7	A	2	c	54400	< 5	400	1x400	0.7	QH	2.2	0.75
8	A	2	c	54940	<10	400	1x400	0.7	QH	2.2	0.75
9	A	2	c	55500	<10	330	1x330	0.7	QH	2.2	0.75
10	A	2	d_1	57290.344 [f_0]	<0.5	330	2x155	0.75	QH	2.2	0.75
11	A	2	d_1	f_0±217	<0.5	78	2x 78	1.2	QH	2.2	0.75
12	A	2	d_2	f_0±322.2±48	<1.2	36	4x 36	1.2	QH	2.2	0.75
13	A	2	d_2	f_0±322.2±22	<1.6	16	4x 16	1.5	QH	2.2	0.75
14	A	2	d_2	f_0±322.2±10	<0.5	8	4x 8	2.4	QH	2.2	0.75
15	A	2	d_2	f_0±322.2±4.5	<0.5	3	4x 3	3.6	QH	2.2	0.75
16	B	3	e	88200	<200	2000	1x2000	0.5	QV	2.2	1.0
17	B	4	f	165500	<200	3000	2x1150	0.6	QH	1.1	1.0
18	B	4	g	183310±7000	<30	2000	2x2000	0.8	QH	1.1	1.0
19	B	4	g	183310±4500	<30	2000	2x2000	0.8	QH	1.1	1.0
20	B	4	g	183310±3000	<30	1000	2x1000	0.8	QH	1.1	1.0
21	B	4	g	183310±1800	<30	1000	2x1000	0.8	QH	1.1	1.0
22	B	4	g	183310±1000	<30	500	2x 500	0.9	QH	1.1	1.0

For a rotating main reflector, the detected polarization vector rotates as the scan reflector rotates. This can be understood by envisioning the detected polarization vector, which is fixed relative to the feedhorn and projected onto the ground below, by simple geometric imaging. The direction indicated in Table 2 as QV (quasi-vertical) corresponds to a direction that lies in the scan plane, while Q" (quasi-horizontal) is the direction that is perpendicular to the scan plane – i.e. in the horizontal plane. At nadir, the two polarizations are of course degenerate, i.e., the observed emissions at V and H polarizations would be identical for an isotropic surface. As the scanner rotates the beam away from nadir, the detected V polarization rotates out of the scan plane, while the detected H polarization rotates out of the horizontal plane in a manner that it is no longer perpendicular to the scan plane. The angle of rotation away from the respective planes equals the scan angle relative to nadir. This is illustrated schematically in Figure 5, which shows the projection of the various polarization vectors
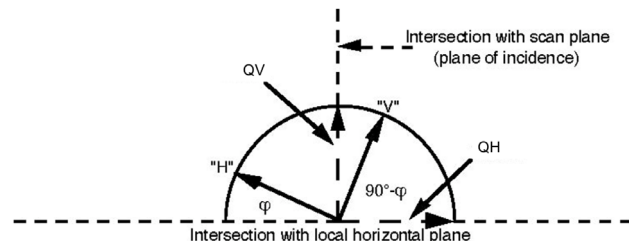

Figure 5. Polarization vectors in the transverse plane

in the plane perpendicular to the ray path - i.e., the plane that contains the electromagnetic field vectors. This plane coincides with the horizontal plane for the nadir scan position but rotates as the scan position changes. In addition, as explained above, the H and V polarization vectors rotate at an angle equal to the scan angle within this plane. When surface emissivity and similar quantities are computed, it is important to perform a correct transformation between the observed H and V vectors and the local true QH and QV vectors.

The antenna reflectors continuously rotate counter-clockwise relative to the direction of spacecraft motion - i.e. the spin vector points in the negative x-direction while the spacecraft moves along the positive x-direction - to complete three revolutions in eight seconds. The scan mechanism is synchronized to the spacecraft clock with a "sync" pulse every 8 seconds, i.e., for every third revolution. Each scan cycle is divided into three segments. In the first segment the earth is viewed at 96 different angles, symmetric around the nadir direction. The antenna is in continuous motion and the 96 samples are taken "on the fly", with each sample representing the mid-point of a brief sampling interval of about 18 ms. The scan speed is such that the corresponding angular sampling interval is 1.11°, i.e., the scan speed is about 61.6°/second. The angular range between the first and last sample centroids is therefore 105.45°, or ±52.725° relative to nadir. The antenna then accelerates and moves to a position between the earth's limb and the spacecraft horizon to point toward an unobstructed view of space. There it resumes the same scan speed as it maintained across the Earth scenes to take four consecutive cold calibration measurements. Next, the antenna is again accelerated to the zenith direction to point toward an internal calibration target that is at the relatively high ambient instrument temperature. It is again slowed down to the same scan speed as it had while taking the Earth scenes in order to take four consecutive warm calibration measurements. Finally, it is accelerated to move to the starting Earth scene position, where it is slowed down to repeat another scan cycle. Every third cycle the synchronization signal arrives just before the start position is reached and is used to maintain this pattern through a phase-locked loop. For JPSS-2+, the scan sync pulse will arrive 2.118 seconds prior to the start position. Figure 6 illustrates a normal operational scan mode. Note that there is also a stare mode, where the antenna can be pointed to the nadir direction or either of the calibration directions for an extended period of time, but that is only used for special purposes. In a normal scan, each of the 96 Earth samples takes about 18 milliseconds, for a total of approximately 1.73 seconds. The "duty cycle" of ATMS is therefore about 65%, i.e. about 65% of the scan cycle period is dedicated to Earth observations.
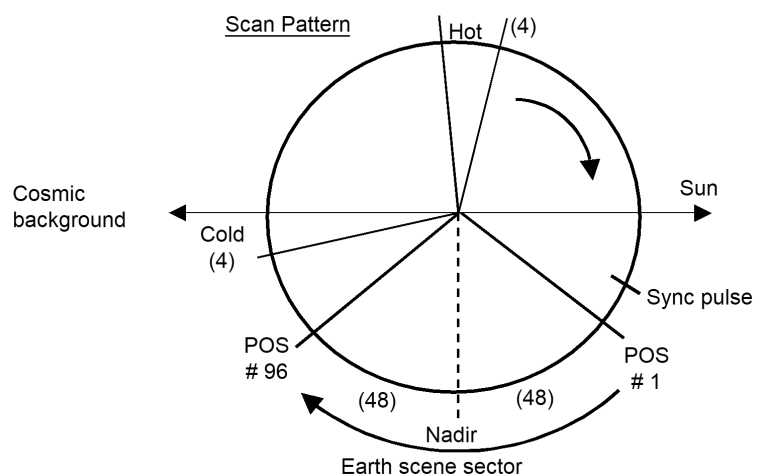

Figure 6. ATMS scan sequence (flight direction is toward the reader)

4. Instrument Noise Characterization

Hersman 1981 identified the noise of total-power radiometers to be characterized in three parts: thermal or intrinsic noise, $1/f^\alpha$ (flicker) noise, and calibration noise. The thermal noise is the Gaussian additive white noise. It has a flat power spectrum. Calibration noise comes from using noisy radiometric measurements of the internal target and cosmic background. Flicker noise comes from the 1/f part of the spectrum, but mitigating calibration noise by filtering radiometric counts across scans can exacerbate the flicker noise contribution. The relationship between total noise, thermal noise, calibration noise, and 1/f noise can be expressed in equation below:

$$NEDT_{total}{}^2 = NEDT_{intrinsic}{}^2 + NEDT_{1/f}{}^2 + NEDT_{calibration}{}^2 \tag{1}$$

4.1 Operational On-orbit NEDT Calculation

The NEDT parameter is a key performance index for microwave sensors. The methods used to compute NEDT can vary between different organizations - e.g., instrument vendors, sensor calibration teams, operational data providers, and NWP centers. In the current operational ATMS sensor data record (SDR) ground processing system, scan-level, channel-dependent NEDT is calculated based on warm load platinum resistance thermometer (PRT) measurements, and warm load and space view counts acquired during four warm load and four cold space view observations, using the following equation.

$$NEDT_{total\_iscan} = \sqrt{\frac{1}{3}\sum_{i=1}^{4}(Counts_{i,iscan} - \overline{Counts}_{iscan})^2} \Big/ Gain_{iscan} \tag{2}$$

In this equation, $Counts_{i,iscan}$ is the individual warm or cold count readings in the same scan, $\overline{Counts}_{iscan}$ is the mean value of warm or cold counts of the same scan, $Gain_{iscan}$ is the calibration gain of the scan obtained using calibration counts and warm load PRT temperatures within the calibration window by the following equation

$$Gain_{iscan} = \frac{\overline{CW}_{iscan} - \overline{CC}_{iscan}}{\overline{TW}_{iscan} - TC} \tag{3}$$

where

$$\overline{CC}_{iscan} = \frac{\sum_{j=iscan-N}^{iscan+N} W_j^{scan\_c}\left\{\frac{1}{n\_samples}\sum_{i=1}^{n\_samples} CC_{i,j}\right\}}{\sum_{j=iscan-N}^{iscan+N} W_j^{scan\_c}} \tag{4}$$

$$\overline{CW}_{iscan} = \frac{\sum_{j=iscan-N}^{iscan+N} W_j^{scan\_w}\left\{\frac{1}{n\_samples}\sum_{i=1}^{n\_samples} CW_{i,j}\right\}}{\sum_{j=iscan-N}^{iscan+N} W_j^{scan\_w}} \tag{5}$$

$$\overline{TW}_{iscan} = \frac{\sum_{j=iscan-n}^{iscan+n} \sum_{i=1}^{N_{PRT}} T^{PRT} W_{i,j}^{PRT}}{\sum_{j=iscan-n}^{iscan+n} \sum_{i=1}^{N_{PRT}} W_{i,j}^{PRT}} \tag{6}$$

In these equations, $CC_{i,j}$ and $CW_{i,j}$ are the cold space and warm load counts, respectively. In operational processing system, the smoothing length, N, for these counts equals 4 for all channels except for channel 17, 21, and 22, in which N equals 2. The parameter n is the number of scans used for warm load PRT smoothing within the calibration window and equals 4 for all channels. N_{PRT} is the number of warm-load PRT readings of each band. For K-, Ka-, and V-bands N_{PRT} is 8; for W- and G-bands N_{PRT} is 7. The normalized weight applied to for each scan of the warm and cold space view counts is given by $W_j^{scan\_w}$ and $W_j^{scan\_c}$, respectively. These weights are re-set to zero for "bad" or "missing" scans. Meanwhile, the weights applied to each PRT temperature, T^{PRT}, in the warm load when computing the warm load temperature is given by $W_{i,j}^{PRT}$. It should be noted that there are four observations each of cold space and the warm load, but the number of samples used, *n_samples*, could be less than four. Once computed, NEDT is output in operational SDR data sets. This method of computing NEDT has been part of the ATMS operational algorithm since the JPSS Integrate Data Processing System Mx_6.0 transition to operations on August 9, 2012.

4.2 Recommended NEDT Calculation

The current operational NEDT development neglects to differentiate between flicker and thermal noise within the total noise. This method is not optimal, so improvements to the NEDT estimation method have been made that distinguish between flicker and thermal noise, while assuming that calibration noise has been optimized by minimizing the total noise through filtering of the radiometric calibration counts, see Equation (17). Total noise can be calculated from the equation below:

$$NEDT_{total} = \sqrt{\frac{1}{2M-1} \sum_{j=1}^{M} \sum_{i=1}^{2} \left(NW_{i,j} - \overline{NW}\right)^2} \tag{7}$$

where

$$NW_{i,j} = TA_{w_{i,j}} - \overline{TW_j} \tag{8}$$

In the equation above, TA is calibrated brightness temperature of warm load and TW is physical temperature of warm load measured from PRTs. TA is calculated from the equation below:

$$TA_{w_{i,j}} = \frac{1}{\overline{Gain_j}} \left(CW_{i,j} - \overline{CC_j}\right) + TC, 1 \leq i \leq 2, 1 < j \leq nscan \tag{9}$$

Where G, CW, CC and TC are calibration gain, warm count, cold count, and cosmic background brightness temperature, respectively. The average calibration and cold space view counts are computed using Equations ((3) through ((6) given in Section 4.1.

The NEDT of thermal noise is calculated from two-sample Allan variance:

$$NEDT_{thermal} = \sqrt{\frac{1}{2M} \sum_{j=1}^{M} \sum_{i=1}^{1} \left(NW_{i+1,j} - NW_{i,j}\right)^2} \tag{10}$$

where M is the total number of scan lines used in calculations. With total noise and thermal noise being known, the 1/f noise can be calculated from the total noise and thermal noise as:

$$NEDT_{1/f} = \sqrt{NEDT_{total}^2 - NEDT_{thermal}^2} \tag{11}$$

Figure 7 below shows the total, thermal and 1/f noise in NOAA-20 ATMS on-orbit measurements. It is seen that thermal noise is dominant across all channels.
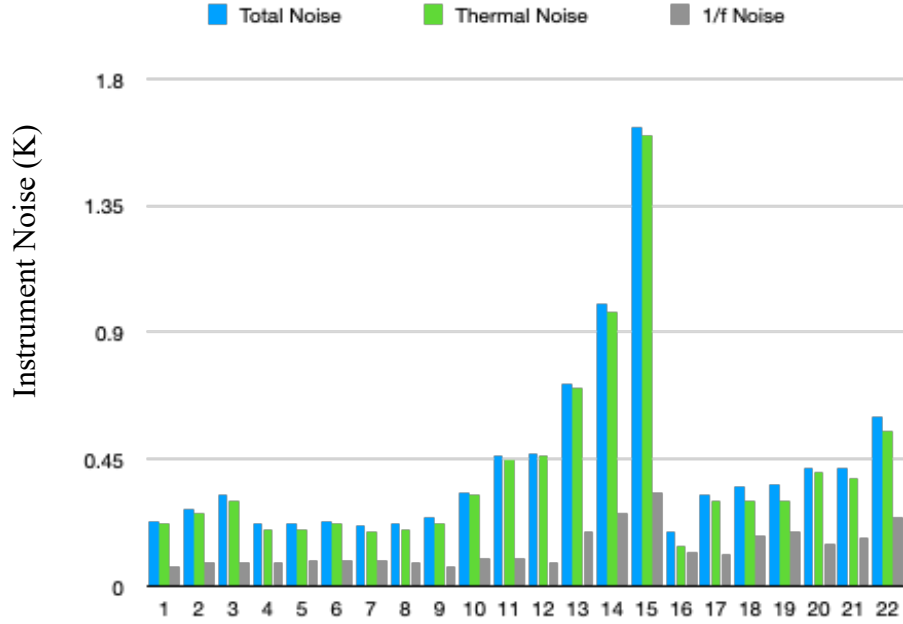
Figure 7. NOAA-20 ATMS on-orbit noise characteristics

Examples of the improvement of the updated NEDT algorithm compared to the current operational algorithm can be visualized in Figure 8 and Figure 9 for NEDT computed from the
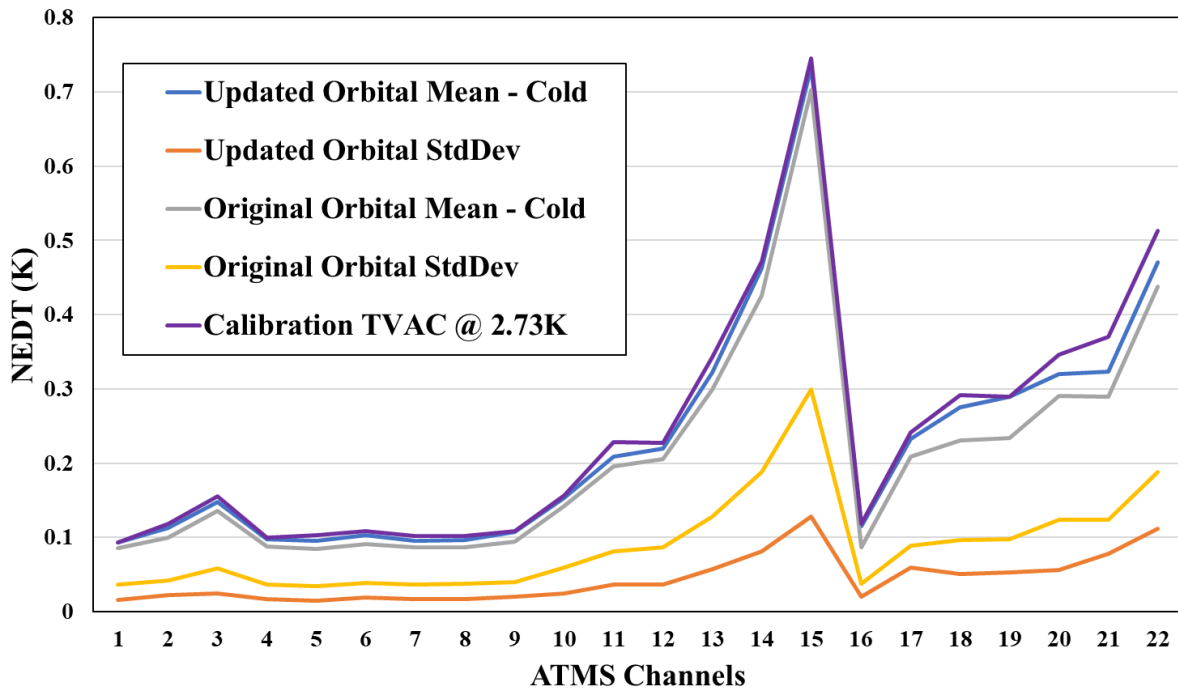
Figure 8. NOAA-20 ATMS cold space view NEDT comparison for orbit number 20490.
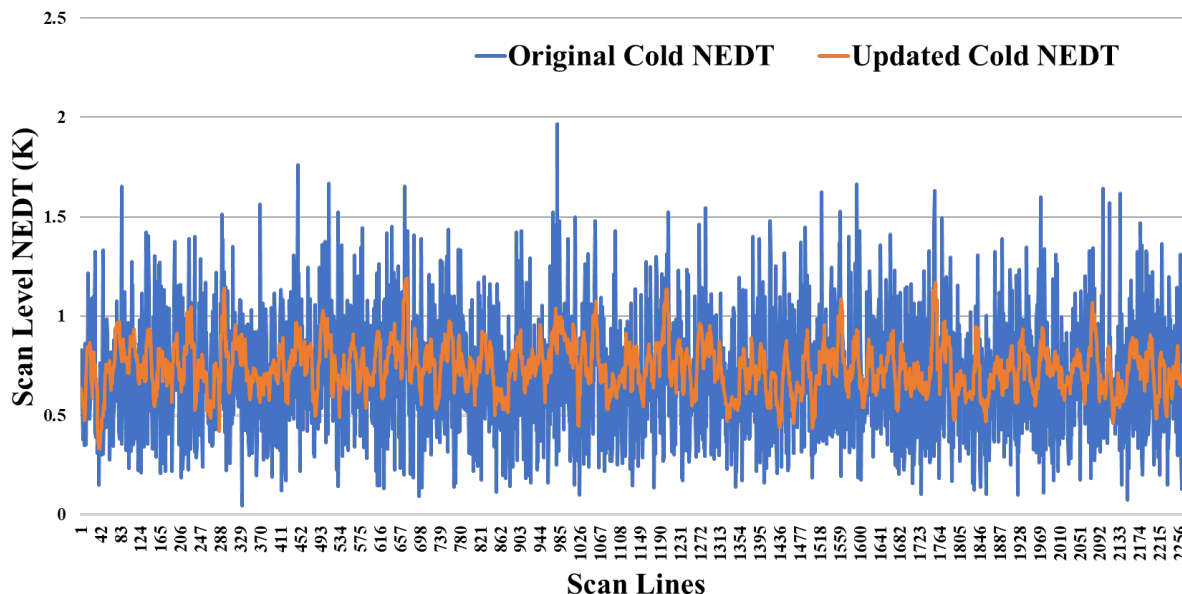
Figure 9. NOAA-20 ATMS Channel 15 scan-level cold space view NEDT by the current operational and updated algorithms for orbit number 20490.

cold space view for NOAA-20 ATMS orbit number 20490. These figures show reduction of NEDT standard deviation in the updated algorithm by about 55% and 45% on average for the KKaV-bands (Chs 1-15) and WG-bands (Chs 16-22) regions, respectively. Note that although this NEDT algorithm is recommended over the current operational algorithm, the recommended algorithm is currently under JPSS Program review at the time of document release.

5. In-flight Calibration System

As described in Section 3, and the scan sequence illustration in Figure 6, each of the two ATMS antenna/receiver systems measures the radiation from two calibration sources during every scan cycle. The first source is the cosmic background radiation emanating from space. Immediately after the Earth has been scanned, the antenna is quickly moved to point in a direction between the Earth's limb and the spacecraft's horizon. There the scan mechanism rotates slowly while four cold space measurements are taken. The second source is an internal blackbody calibration target (often called a "warm load"), which is at the ambient internal instrument temperature. After the space calibration view, the antenna is quickly moved to point in the zenith direction, where the blackbody target is located. Again, the antenna scans slowly while four warm target measurements are taken. Thus, cold and warm calibration measurement populations that bracket the Earth scene measurements are obtained for every scan cycle.

Such an end-to-end calibration system allows most of the system losses and instrument defects be calibrated, since the calibration measurements involve the same optical and electrical signal paths as Earth scene measurements. The only exception is that the internal calibration target appears in the antenna near field and can reflect leakage emission from the antenna itself. However, this effect is taken into account with so-called "bias corrections" in the calibration processing. The end-to-end calibration system is beneficial to the calibration process compared to a calibration system that uses switched internal noise sources injected into the signal path after the antenna. On the other hand, this benefit is accompanied by the cost of significant weight gain, since the internal calibration target is fairly massive.

The purpose of the calibration measurements is to accurately determine the radiometer transfer function, which relates the measured digitized output - i.e., the instrument counts, C - to the associated radiance, which can be expressed as follows:

$$R = F(C) \tag{12}$$

This counts-to-radiance transfer function is illustrated schematically in Figure 10. In this figure, the subscripts c and w refer to the cold and warm calibration points, respectively, and the subscript s refers to an Earth scene. This function depends primarily on channel frequency and instrument temperature. The radiometer transfer function could also undergo short term and long-term changes due to gain fluctuations and drift due to aging and other effects. The units of radiance are mW/m²-sr-cm⁻¹.

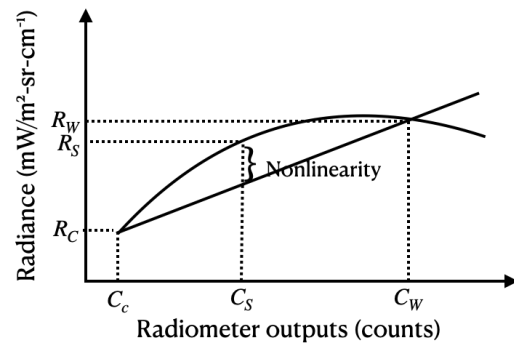Figure 10. Calibration transfer function illustration.

If the transfer function were perfectly linear, then the form of the calibration equation can be given by

$$F_{lin}(C) = a_0 + a_1 C \tag{13}$$

In this equation, any two calibration points could be used to uniquely determine its form - i.e., the two linear coefficients, a_0 and a_1 - at the time of the calibration measurements. While it has been

a requirement in radiometer instrument design to make the transfer function as linear as possible, it is slightly nonlinear in reality. This is depicted in the illustration shown in Figure 10. To account for the slight nonlinearity a quadratic, or $a_2 C^2$, term is added to the above equation to give

$$F_{nonlin}(C) = a_0 + a_1 C + a_2 C^2 \triangleq F_{lin}(C) + Q(C). \tag{14}$$

More details about the radiometer transfer function are given below.

The ATMS radiometric calibration equation can be expressed with the following equation:

$$R = R_c + (\overline{R_w} - R_c)\left(\frac{C_s - \overline{C_c}}{\overline{C_w} - \overline{C_c}}\right) + Q, \tag{15}$$

where $\overline{R_w}$ and R_c are the warm and cold calibration target radiance corresponding respectively to the warm and cold target temperatures (T_w and T_c). The parameters $\overline{C_w}$ and $\overline{C_c}$ are respectively the mean warm and cold counts; C_s is the scene count; and Q is the calibration non-linearity term.

$$Q = \frac{1}{4} T_{nlin}^{max}\left[4\left(\frac{C_s - \overline{C_c}}{\overline{C_w} - \overline{C_c}} - 0.5\right)^2 - 1\right] \tag{16}$$

As mentioned earlier, each of the two calibration targets - i.e., the warm load and cold space - is sampled four times in succession. The measurements are in the unit of digital "counts," which represent the radiometer's output. It is assumed that the radiative environment does not change between successive samplings, so that any differences between the measurements are strictly due to noise, which can be reduced by averaging or smoothing the measurements.

For ATMS, averaging or smoothing the measurements is implemented by computing a count averaged over the four in-scan samples and over several scans. Ancillary tables are used to specify the respective weights. From Suomi-NPP ATMS on-orbit data, it was found that there was striping noise (1/f flicker noise) in the along-track direction. In the operational processing system, calculations of the average of warm target radiance and counts, $\overline{R_w}$ and $\overline{C_w}$, and cold space counts, $\overline{C_c}$, depend on the weighting coefficients as well as the number of scan lines involved in the averaging - i.e., $2N_s+1$. The averaging interval in the time domain (e.g. number of scan lines) is determined from a power spectrum analysis of the warm and cold counts which determine the location of 1/f "knee". The calibration counts of all ATMS channels are averaged using a triangular function as follows:

$$W_k = \frac{1}{N_s + 1}\left(1 - \frac{|k|}{N_s + 1}\right). \tag{17}$$

For ATMS on-orbit calibration, $N_s = 9$ was chosen for Channels 1-15 and 18-20 and $N_s = 5$ for Channels 17, 21 and 22. The average calibration counts for the ith scan of a given channel can be calculated as:

$$\overline{R_w}(i) = \sum_{k=i-N_s}^{i+N_s} \sum_{j=1}^{4} W_{k-i} R_w(k, j) \tag{18}$$

$$\overline{C_w}(i) = \sum_{k=i-N_s}^{i+N_s} \sum_{j=1}^{4} W_{k-i} C_w(k,j) \tag{19}$$

$$\overline{C_c}(i) = \sum_{k=i-N_s}^{i+N_s} \sum_{j=1}^{4} W_{k-i} C_c(k,j) . \tag{20}$$

In current radiometric calibration algorithm, radiance is calculated from Planck's law as a function of frequency:

$$R(v,T) = \frac{2hv^3}{c^2} \frac{1}{e^{\frac{hv}{kT}} - 1} . \tag{21}$$

In the equation above, the Planck's constant, h, is $6.626070040 \times 10^{-34} \, J \cdot s$ and v is frequency in Hz. Meanwhile, the speed of light, c, has a value of $2.99792458 \, m/s$, the Boltzmann constant is given by $k = 1.38064853 \times 10^{-23} J/K$, and T is temperature in units of K. The unit of radiance from this equation is $J \cdot s^{-1} \cdot m^{-2} \cdot sr^{-1} \cdot Hz^{-1}$. Considering that power is equivalent to energy expended per unit time, $W = J \cdot s^{-1}$, the unit of radiance becomes the NIST standard of $W \cdot m^{-2} \cdot sr^{-1} \cdot Hz^{-1}$. To transfer the radiance from per frequency interval to per wavelength interval, the following equation must be applied:

$$R_\lambda(\lambda, T) = \frac{c}{\lambda^2} R_v \left(\frac{c}{\lambda}, T \right) \tag{22}$$

In the equation above, λ is the wavelength. In addition, to make the radiance values more convenient to store and use, a factor of 10 is need to be applied to transform the radiance units from $W \cdot sr^{-1} \cdot m^{-3}$ to $mW \cdot m^{-2} \cdot sr^{-1} \cdot cm^{-1}$.

Since the primary ATMS TDR and SDR product is brightness temperature in units of K, the retrieved radiance after correction needs to be converted to brightness temperature using Plank's Function. The following subsections sequentially discuss how the warm and cold calibration points are obtained, and the sources of radiance measurement errors and uncertainties. Discussion of the methods used to perform the radiance corrections are given in Section 6.

5.1 Blackbody View

The internal calibration targets (also referred to as warm loads) are approximately cylindrical in outline and are made up of pyramid shaped metal structures coated with an absorbing material. Figure 11 shows the ATMS calibration target for the K-, Ka-, and V-bands (KAV target); a similar target is used for the W- and G-bands (WG target). For the larger aperture, the pyramids are about 1 cm across and about 4 cm high. The use of metal for the base and core ensures that temperature gradients across the targets are minimal, while the pyramid structure and the absorbing coating ensure that the emissivity is close to 1 ($\varepsilon \geq 0.9999$). The target is surrounded by a metal shroud that mates very well with a matching shroud surrounding the rotating reflector antenna in order to prevent stray radiation from external sources to affect the warm calibration measurements. For ATMS, its

Figure 11. Photo ATMS KAV Warm Load

antenna moves during calibration measurements, the calibration target is slightly larger than the antenna shroud aperture, so that the antenna has a full view of the target during the entire calibration period.
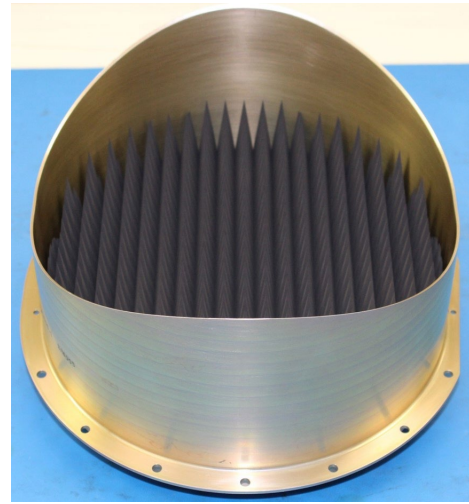
In order to reduce the effect of random noise, the calibration target is consecutively viewed four times. Note that consecutive samplings are used in lieu of a single sampling of longer duration in order to keep the data collection control system simple. The effective calibration measurement noise, after averaging, is then reduced by a factor of two below the NEDT values listed in Table 2. These values can be further reduced by averaging over several calibration cycles, as was described earlier. On-orbit evaluation results show that the four consecutive measurements are kept highly consistent.

The emissivity of the calibration targets is required to be at least 0.9999. This is necessary in order to keep radiation that is unavoidably emitted from the radiometer's local oscillators through the antenna and reflected back from the calibration target to a minimum. For example, such radiation could masquerade as a radiated brightness temperature of as much as 100 K. An emissivity of 0.9999, and thus a reflectivity of 0.0001, would then yield a reflected contribution of 0.01 K

The targets are not actively thermally controlled, but the ATMS interface with the spacecraft is. The entire ATMS instrument is thermally insulated from the target mounting platform. In addition, being insulated from external thermal swings, the target temperatures will not change rapidly (less than 0.001 °C/sec) and temperature gradients across the targets will be small (less than ±0.05 °C). To ensure good knowledge of the target temperatures, there are eight and seven temperature sensors (PRTs) embedded throughout the KAV and WG targets, respectively. Measurement accuracy is better than 0.1°C. The PRTs are embedded in the metal structure from the back and are close to the coated front surface.

The vertical temperature gradient in the pyramid structure is not measured and difficult to model and predict. Radiation at the shorter wavelengths may originate from a particular part of the pyramids while longer wavelengths may originate from a different area – e.g., tips vs. troughs.

There are indications from previous studies that such gradients can influence calibration accuracy. Temperature gradients in a periodic structure as in the ATMS targets can also cause resonant effects such as grating "sidelobes." On-orbit results show that the variation of warm load temperature is less than 0.2K per orbit, and temperature gradient within the target is less than 0.05K.

In general, there could be a small difference between the radiance computed from the physical temperature of the target and the estimated emissivity and the radiance inferred from the radiometer output, which can be caused by effects such as discussed above. One of the objectives of the ground based thermal-vacuum measurements, where operational conditions are simulated as closely as possible, is to determine the magnitude and biases of such differences.

5.2 Cold Space View

There are four cold space calibration beam groups located at 6.66°, 8.33°, 10.00°, and 13.33° below the anti-sun direction towards nadir in the scan plane. Which beam group to use is determined by post-launch test results, but to date has always resulted in the 6.66° group. Within a beam group, the cosmic background radiation is sampled four times consecutively, with two neighboring samples being spaced 1.11° apart. However, the radiative environment for the cold space view is much more complicated than for the warm calibration target view. Although the cosmic radiometric temperature is well-known (e.g., 2.726 ± 0.004 K), significant radiation from the Earth as well as Earth radiation reflected from spacecraft structures can enter the radiometer receiver through the antenna sidelobes. Figure 12 provides a conceptual illustration. For example, we can estimate an uncertainty on the order of 0.1-0.2 % resulting from the radiance that is received within the 124° sector that "sees" Earth from an 828 km orbital altitude of JPSS (the orbital altitude for Suomi NPP is 824 km). This contribution corresponds to 0.25-0.5 K, which is about 1/10 to 1/5 of the cosmic radiation. This is not insignificant. But the impact on calibration accuracy is relatively small, which is discussed in the next section. Contributions due to reflections from the structures and surfaces on the spacecraft are probably minor. Radiation emitted from the spacecraft is expected to be negligible, since most surfaces will be covered with MLI blankets – a metallized Mylar material that is highly reflective at microwave frequencies.
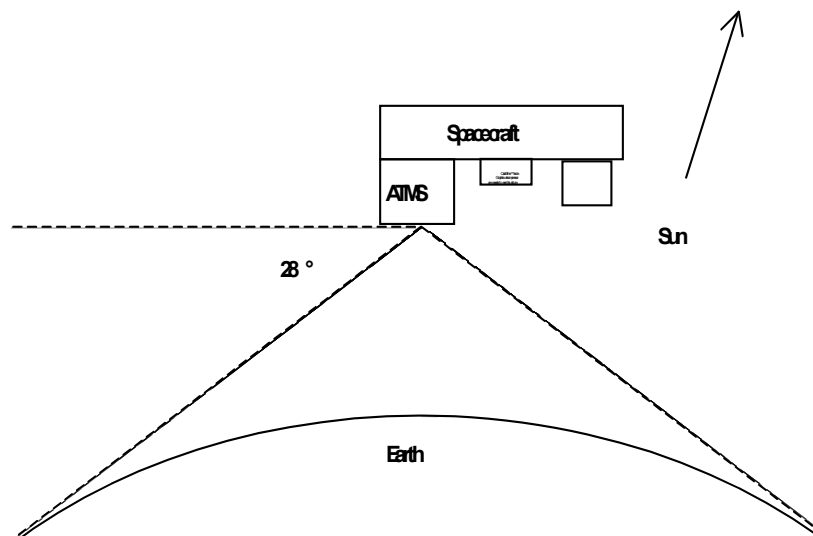

Figure 12. Space view geometry
(flight direction is toward the reader, out of the page)

Figure 12 also suggests that the Earth sidelobe radiation probably depends on the exact pointing direction and is likely to be greatest when the antenna boresight is closest to the Earth. This means that, for a given nominal space calibration position, the sidelobe contribution may vary between the four consecutive samples, which cover an angular range in excess of 4°. The baseline algorithm averages these together to reduce the effective noise. An additional analysis shall be undertaken to determine an on-orbit correction.

Finally, one should note that the cold space view could also be contaminated by a lunar intrusion. For a few days a month and for most of the months in a year, the Moon will enter the Field of View of ATMS space view scan. For SNPP and NOAA-20, the Moon phase is in 80^0 to 110^0 range when it is seen from the spacecraft. Moon radiance may approach the field of view of one or more of the space view positions. In the worst case, when the Moon is exactly in the boresight direction, Moon radiance can increase the space view brightness temperature by up to 30 K for the channels with a 1.1° FOV, up to 5 K for the channels with a 2.2° FOV and 1 K for the channels with a 5.2° FOV. When this happens, it is necessary to either account for the increase in space view radiance, i.e., model it, or find the "clean" cold counts for calibration. Details of the lunar intrusion correction are given in the next section.

5.3 Sources of Errors and Uncertainties

This section summarizes the sources of errors and uncertainties in the calibration process. Calibration errors can be classified as bias errors and random errors associated with measurements of the calibration targets and other sensor/spacecraft hardware – e.g., warm load temperature gradients and emissivity, cold space temperature, antenna surface emissivity, antenna pattern gain, satellite surface reflectivity, etc. - used to determine coefficients needed in the calibration process. The bias errors are considered static and independent, and thus can be compensated for by direct addition of bias corrections. The random errors are uncertainties due to instrument characteristic fluctuations that are assumed to be random and independent, and can be added up in a root-sum-squared (RSS) sense. This is not strictly correct – e.g., biases may vary with time, and the nature of "random" fluctuations may have some correlation with the behavior of other instrument or spacecraft system components - but the resulting errors in the ATMS uncertainty estimates are judged to be relatively small. Theoretically speaking, all known biases can be removed by first principle calibration factors, so that only the random uncertainties remain.

As was explained at the beginning of this section, the on-orbit calibration concept consists of initially determining the radiance from the linear part of the transfer function with support of data from two calibration points, the cold space calibration view and the internal blackbody calibration view. The linear radiance is then adjusted with bias corrections, where the non-linear correction shown in Equation (15) is one of those corrections. The corrected radiances are converted to antenna brightness temperatures using the Planck function to generate the ATMS Temperature Data Record; and these antenna brightness temperatures are subsequently corrected for signal contamination through the antenna pattern sidelobes to create the ATMS Sensor Data Record scene brightness temperature values. The absolute accuracy of this scene brightness temperature is termed the calibration accuracy. The calibration accuracy is strictly defined as the mean difference between the inferred and the actual brightness temperature.

In a similar way that ATMS calibration generates a radiance that can be converted into a brightness temperature using the Planck function, the calibration accuracy can be estimated as a radiance accuracy that can be converted into a brightness temperature accuracy with the aid of the derivative

of the Planck function with respect to the brightness temperature. Radiance calibration accuracy can be expressed as

$$\Delta R = \text{RSS}\{x\Delta R_w;\ (1-x)\Delta R_c;\ x(x-1)\Delta R_{NL};\ \Delta R_{reflEmis};\ \Delta R_{sys}\}, \qquad (23)$$

where "RSS" means that the result is the square root of the sum of the squares of the terms. The factor $x = \big(R(T_s) - R(T_c)\big)/\big(R(T_w) - R(T_c)\big)$, and $\Delta R_w, \Delta R_c, \Delta R_{reflEmis}$ and ΔR_{NL} are the respective uncertainties in the calibration target radiance, reflector emissivity, and nonlinearity amplitude. The term ΔR_{sys} is an uncertainty due to random instrument fluctuations - e.g., gain fluctuations. Note that Equation (22) expresses the uncertainty only and no biases are included in it.

Although scene temperatures may be as low as 80-90 K at the high frequencies due to scattering from precipitation, the meaningful operational dynamic range is 200-300 K for sounding channels and about 140-300 K for window channels. With a T_w on the order of 300 K and T_c close to zero, the meaningful dynamic range of x is 2/3 to 1 for the sounding channels. In the worst case, $x \sim 2/3$, the relative weights of the first two terms in Equation (22) are then 4/9 and 1/9, respectively. This means that if $\Delta R_w = \Delta R_c$, errors in T_c contribute four times less to the overall calibration accuracy than errors in T_w, and are considerably less than that for most scenes. It is useful to keep this perspective in mind when the error sources are discussed.

In the following, the sources contribute to the above uncertainties are briefly discussed.

5.3.1 Blackbody error sources
This error stems from *uncertainty* in the knowledge of the following five factors:
a) blackbody emissivity,
b) blackbody physical temperature,
c) reflector/shroud coupling losses,
d) reflector emission, and
e) reflected local-oscillator leakage.

Of these, the second term is expected to dominate.

The *blackbody emissivity* is generally known to be in a range of [ε_{min}, 1.0]. A typical value for ε_{min} is 0.99993. Due to limited measurement accuracy, the emissivity should be interpreted as

$$\varepsilon = 1.0 - (1.0 - \varepsilon_{min})/2 \pm \Delta\varepsilon, \qquad (24)$$

where $\Delta\varepsilon$ is the estimated uncertainty. It is bounded by $(1.0 - \varepsilon_{min})/2$. For the example quoted, where ε_{min} is estimated to be 0.99993, an uncertainty of less than 0.000035 would be estimated. An alternative estimate could be based on an analysis of the measurements of the reflectivity that can be used to determine the emissivity.

The *blackbody physical temperature* uncertainty contributes to blackbody radiance uncertainty through the following four factors:
a) surface temperature drifts between the time of temperature measurement and the time of radiometer measurement ($\Delta R(T_{drift})$),
b) horizontal temperature gradients in the blackbody ($\Delta R(T_{H\_grad})$),

c) temperature measurement uncertainties ($\Delta R(T_{meas})$), and
d) vertical temperature gradients and uncertain origin of the radiation ($\Delta R(T_{V\_grad})$).
The last factor is currently unknown, but could dominate the blackbody physical temperature uncertainty.

The *reflector/shroud coupling losses* occur because the antenna and blackbody shrouds do not mate perfectly, and external radiation (from the interior of the instrument) will enter the antenna through the gap between the shrouds. This effect is uncertain because of uncertainties in measuring and modeling the coupling losses as well as uncertainties in the knowledge of the external radiation. The magnitude of this is expected to be very small and can be ignored.

The *reflector emission* radiance uncertainty is dictated by uncertainties in determining the amount of radiance emission from the ATMS antenna. It is mainly driven by uncertainties in the knowledge of the antenna emission and the reflector and blackbody radiance difference. Since this term is dominated by the product of the reflector and blackbody radiance difference - given an approximately 10 K brightness temperature difference - and the emission uncertainty (~0.003), then this effect can be considered negligible. See the "antenna emission error sources" subsection further below for more detail.

Finally, the *leakage* signal originating from the local oscillators (LOs) and emitted by the antenna may be reflected back to the antenna, if the warm load emissivity is not unity - i.e., if its reflectivity is not zero. This is uncertain because both the leakage signal and the target reflectivity, or emissivity, are not precisely known. The latter is expected to dominate, and the former can be ignored. The reflected LO signal may also interfere with itself by changing the operating point of the detector system, which then impacts the intrinsic noise level of the amplifier. Thus, although the LO interference may be well outside the IF passband and therefore not directly measurable, it can still significantly impact the apparent output noise of the system.

The resulting uncertainty is

$$\Delta R_w = \text{RSS} \begin{Bmatrix} \Delta \varepsilon R(T_w); \ \Delta R(T_{\text{drift}}); \ \Delta R\left(T_{H_{\text{grad}}}\right); \\ \Delta R(T_{\text{meas}}); \ \Delta R\left(T_{V_{\text{grad}}}\right); \ \Delta \varepsilon R(T_{\text{LO}}) \end{Bmatrix}, \qquad (25)$$

where T_{LO} is the local oscillator brightness temperature.

Only the first term is expected to change on orbit, so this can be contracted to

$$\Delta R_w = \left\{ [\Delta \varepsilon R(T_w)]^2 + \left[\Delta R\left(T_{w,fixed}\right)\right]^2 \right\}^{1/2}, \qquad (26)$$

where the term $\Delta T_{w,fixed}$ represents the unchanging terms compiled from ground measurements.

5.3.2 Cold calibration (space view) error sources
This error stems from uncertain knowledge of the following four factors:
a) Earth contamination through the antenna sidelobes,
b) spacecraft contamination through the antenna sidelobes,
c) reflector emission, and
d) cosmic background temperature.

The *sidelobe contamination* is uncertain due to uncertain knowledge of the antenna pattern (i.e., sidelobes) as well as uncertain knowledge of the radiation from Earth and the spacecraft. The latter consists mostly of reflected Earth radiation, since most visible surfaces will be covered by

reflective materials, as discussed above. Both effects may be modeled and pre-computed, but the associated uncertainties are expected to be substantial. This is the largest contribution to this term.

We may express the sidelobe radiation as the product of an effective antenna efficiency, a_{eff}, which is defined over the sector that receives this radiation, and an effective scene radiance for that sector, R_{eff}:

$$R_{\text{SL}} = a_{\text{eff}}R_{\text{eff}} . \tag{27}$$

The uncertainty is then the first-order variation of R_{SL}:

$$\Delta R = \text{RSS}\{\Delta a_{\text{eff}}R_{\text{eff}};\ a_{\text{eff}}\Delta R_{\text{eff}}\} . \tag{28}$$

The uncertainty in a_{eff}, is primarily due to uncertain antenna patterns from which it is usually computed, and the uncertainty in R_{eff} is primarily due to an uncertain or variable mean radiance of the visible Earth disc. There is also an error component caused by representing the sidelobe radiation as the simple product shown in Equation (26). In reality the right-hand-side of Equation (26) involves a double integral, i.e., a convolution between the two variables. It may be noted that the effective scene radiance varies along the orbit. There are latitudinal (i.e., intra-orbital), longitudinal (i.e., inter-orbital), and temporal (e.g., inter-seasonal) variations in the effective radiance of the visible portion of the Earth. In Equation (26) shown above these effective radiance variations are ignored but they may be modeled or estimated.

The *reflector emission* radiance uncertainty is dictated by uncertainties in determining the amount of radiance emission from the ATMS antenna. It is mainly dictated by uncertainties in the knowledge of the antenna emission and the reflector and cold space radiance difference. Since this term is dominated by the product of the reflector and cosmic background radiance difference - given an approximately 270 K brightness temperature difference - and the emission uncertainty (~0.003), then this radiance uncertainty can be quite substantial, translating to a brightness temperature uncertainty of about 0.8 K. See the "antenna emission error sources" subsection further below for more detail.

Finally, although the *cosmic background temperature* is well known, there is an uncertainty associated with it. However, it can be ignored here, since the uncertainty of the sidelobe radiation and antenna emission are expected to dominate the cold calibration uncertainty. The result is

$$\Delta R_{\text{c}} \approx \Delta R_{\text{SL}} = \text{RSS}\{\Delta a_{\text{eff}}R_{\text{eff}};\ a_{\text{eff}}\Delta R_{\text{eff}};\ \Delta R_{\text{reflEmis}}\} . \tag{29}$$

5.3.3 Antenna error sources

Due to the coating material used, the rotating plane reflector is not lossless and has its own thermal emission. According to the Niels Skou's equation, at microwave frequencies the emissivity of a good conducting surface, viewed at normal incidence, is

$$\epsilon_N = \frac{1}{15}\sqrt{\frac{f}{\sigma \cdot 10^7}} , \tag{30}$$

where *f* is the receiver microwave frequency and σ is the conductivity of the reflecting surface. This equation is considered valid for perfectly smooth and pure bulk conductive materials. For example, for bulk gold ($\sigma = 4 \times 10^7$) the equation gives 0.0014 at 183 GHz and 0.0005 at 23.8 GHz. However, the actual emissivity of real reflector surfaces is invariably greater than the

computed theoretical value, due primarily to surface roughness and impurities. The ATMS flight reflector is made of Beryllium that is given a nominally 0.6-micron gold plating layer, which has been electroplated on a Nickel interfacing layer. Since the gold plating thickness is comparable to the skin depth, and is likely to have extreme microscopic granularity and roughness, it is not unexpected that the emissivity would greatly exceed the values computed from the Skou's equation in low frequency band.

Soon after the launch of Suomi-NPP ATMS, pitch maneuver observations revealed that the rotating flat reflector of ATMS has a polarization-dependent reflectivity. Based on Fresnel reflection theory, a fully-polarized physical model for antenna reflection was established (Yang et.al., 2016). The vector expression of radiation emitting from the reflector surface, R_Q, is

$$R_Q = \begin{bmatrix} R_{Qv} \\ R_{Qh} \\ R_{Q3} \\ R_{Q4} \end{bmatrix} = \begin{bmatrix} R_s + \epsilon_h(R_{rfl} - R_s) + (R_{rfl} - R_s)(\epsilon_v - \epsilon_h)sin^2\theta \\ R_s + \epsilon_h(R_{rfl} - R_s) + (R_{rfl} - R_s)(\epsilon_v - \epsilon_h)cos^2\theta \\ (R_{rfl} - R_s)\epsilon_h(1 - \epsilon_h)sin2\theta \\ 0 \end{bmatrix}. \qquad (31)$$

In Equation (30) above, R_s and R_{rfl} represents the scene and antenna reflector radiance, and ϵ_h and ϵ_v are the reflector emissivity at H and V polarization. Note that antenna reflector emissivity is related to reflectivity with the expressions, $\epsilon_h = (1 - r_h)$ and $\epsilon_v = (1 - r_v)$, where the relationship between the V- and H-polarization coefficients is $r_h^2 = r_v$. In addition, the reflector scan angle is given by the parameter θ. When the reflector scans to cold space, $R_s = R_c$, and when it scans to the calibration blackbody target, $R_s = R_w$. The uncertainty of H- and V-polarization radiation emitting from the antenna surface, ΔR_Q, is then related to the uncertainty in these variables. If the uncertainty related to the scan angle is considered negligible, this uncertainty can be expressed as follows:

$$\Delta R_{Qv} = RSS\{\Delta R_s; \Delta\epsilon_h(R_{rfl} - R_s)(1 - sin^2\theta); \epsilon_h\Delta(R_{rfl} - R_s)(1 - sin^2\theta); \Delta\epsilon_v(R_{rfl} - R_s)sin^2\theta; \epsilon_h\Delta(R_{rfl} - R_s)sin^2\theta\} \qquad (32)$$

$$\Delta R_{Qh} = RSS\{\Delta R_s; \Delta\epsilon_h(R_{rfl} - R_s)(1 - cos^2\theta); \epsilon_h\Delta(R_{rfl} - R_s)(1 - cos^2\theta); \Delta\epsilon_v(R_{rfl} - R_s)cos^2\theta; \epsilon_h\Delta(R_{rfl} - R_s)cos^2\theta\}. \qquad (33)$$

The uncertainties related to the scene, e.g., either the cold or warm blackbody, have been discussed in the previous subsections. Meanwhile, the antenna reflector temperature is modeled and not measured, and the antenna emissivity is estimated from analysis of satellite pitch maneuver data where the ATMS views cold space over several scans in what is normally the Earth sector view.

5.3.4 Instrument (transfer function) error sources
This error stems from uncertainty in the knowledge of the following four factors:
a) nonlinearities,
b) system noise,
c) system gain drift, and
d) bandpass shape changes.

The *nonlinearities* can be modeled as a quadratic term that is a function of cold space and warm load radiances, and cold space, warm load, and scene counts. This quadratic nonlinearity correction, described in Section 6.5, is only an approximation and is therefore uncertain. In

addition, cold space and warm load radiances, and cold space, warm load, and scene counts are not known precisely. However, they are ignored as small variations in them are insignificant to the estimate of the magnitude of the nonlinearity.

The system terms are due to random fluctuations and are characterized in terms of standard deviations. They are channel dependent, as are most of the effects discussed above. The combined effect is expressed as ΔR_{sys} in Equation (22).

6. Calibration Processing Steps

In this section we describe how the on-board calibration measurements are used to first determine the calibration coefficients, as discussed in Section 5, and then applied to compute estimated scene radiances, which are subsequently bias corrected and finally converted to antenna temperature and scene brightness temperature products. In summary, the procedure is illustrated in Figure 13.
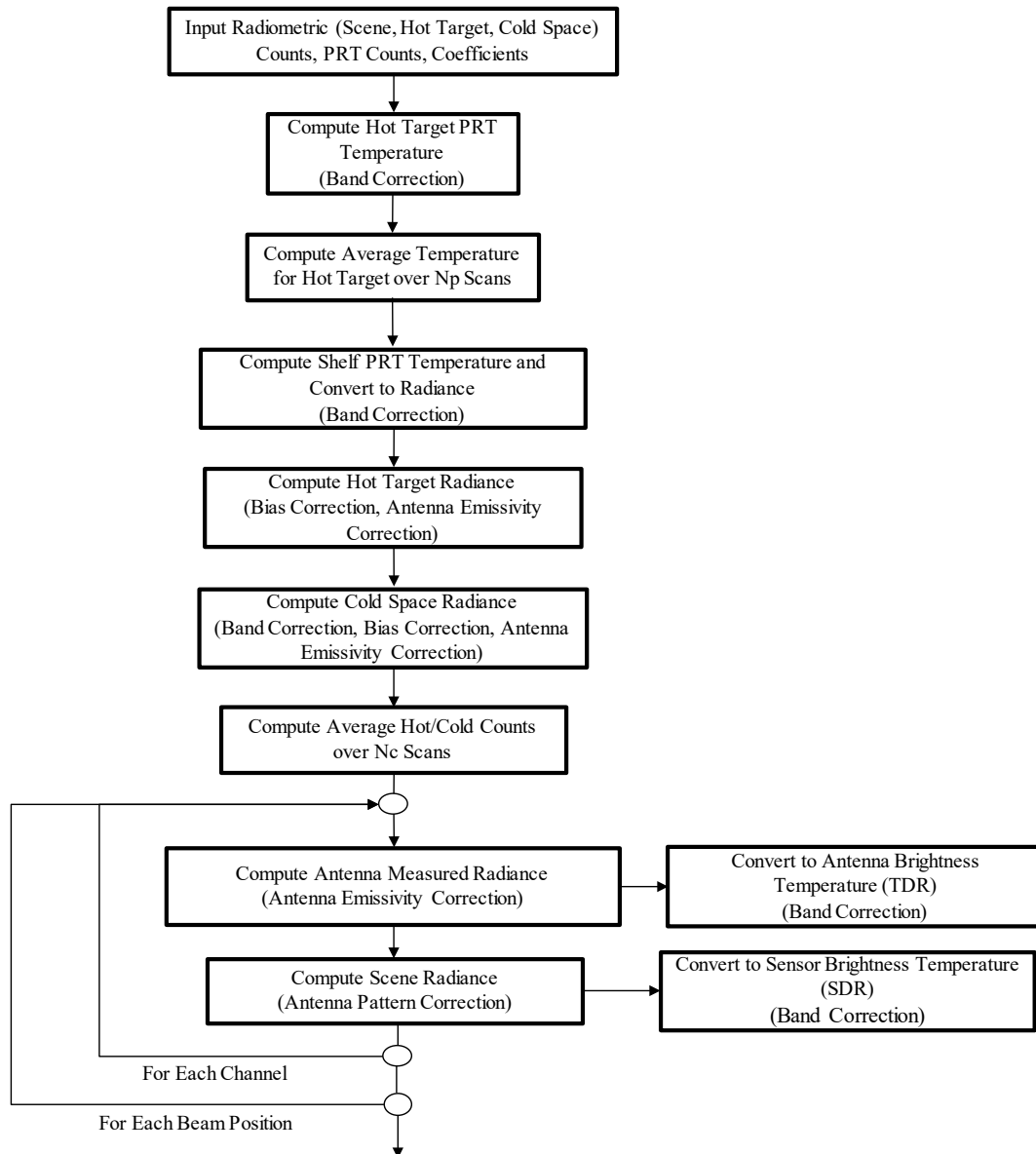
Figure 13. ATMS TDR and SDR algorithm flow chart

Several calibration steps are required to convert a PRT raw count to a corresponding physical temperature. The procedure for such conversions is common to all PRTs. In essence, a PRT is a passive sensor with a resistance, $\Re$, that is a known function of temperature. An analog-to-digital converter (ADC) outputs a digital 'count' that is proportional to the resistance, which is inserted

into the telemetry. The conversion to temperature on the ground consists of two steps. In the first step, the resistance is reconstructed with a linear transfer function that is calibrated with on-board measurements of a known reference resistor (the precision analog monitor – PAM). This conversion is

$$\mathfrak{R}_{\text{PRT}} = \mathfrak{R}_{\text{PAM}}\,(C_{\text{PRT}} - C_{\text{off}})/(C_{\text{PAM}} - C_{\text{off}}) \tag{34}$$

where C_{off} refers to a reference count with shorted inputs (i.e., zero resistance). Thus, the essentially linear ADC is "calibrated" on-board with two reference measurements, just as is done for the slightly nonlinear radiometer.

The second step is to convert the resistance to a temperature value. Here, the transfer function – called the Callendar-Van Dusen equation – is nonlinear:

$$\mathfrak{R}_{\text{x}} = \mathfrak{R}_0\{1 + \alpha[T_{\text{x}} - \delta(T_{\text{x}}/100 - 1)(T_{\text{x}}/100) - \beta(T_{\text{x}}/100 - 1)(T_{\text{x}}/100)^3]\} \tag{35}$$

where $\mathfrak{R}_0$, α, β and δ are characteristic coefficients and are determined by the manufacturer for each individual PRT. The temperature T_{x} in Equation (34) is in unit °C. This equation is solved for T_{x} by the Newton-Raphson iteration. A simpler but less robust alternative approach, used with the AMSU systems, is to fit a cubic polynomial, $T = c_0 + c_1 C + c_2 C^2 + c_3 C^3$, to the two functions expressed in Equations (33) and (34).

Using this method, all PRT readings are converted to temperatures.

6.2 Spectral Response Function and Band Correction

In radiance calibration, the warm load calibration target needs to be transformed to radiance by using the Planck function shown in Equation (20). During the process, the spectral response functions (SRFs) for different ATMS receiver bands need to be considered. For the purpose of creating a functional relationship between antenna subsystem hardware spectral brightness temperature, T, and band-corrected brightness temperature, T', the band-corrected radiance is computed, based on receiver outputs, by integrating the product of spectral radiance, R, and normalized spectral response function, S, over the range of measured frequencies:

$$R' = \int_{v_1}^{v_2} R(v, T)S(v)\,dv \tag{36}$$

By using the equation above, the radiance was calculated for spectral brightness temperatures ranging from 2.7K to 330K using normalized receiver SRFs for each of the 22 ATMS channels. The associated band-corrected brightness temperature can then be calculated from the inverse Planck function below:

$$T' = \frac{h \cdot v_0}{k \cdot ln\left(\frac{2hv_0^3}{c^2 R'} + 1\right)}. \tag{37}$$

The parameters of the above equation have been defined in Equation (20) of Section 5. With the accumulated data, for each ATMS channel a relationship can then be established to transfer between spectral brightness temperature, T, and band-corrected brightness temperature, T':

$$T' = c_0 + c_1 \cdot T . \tag{38}$$

Table 3 and Table 4 list the coefficients c_0 and c_1 calculated by using ATMS SRF measurements.

Table 3. ATMS Band Correction Coefficient c_0

Ch. No.	Center Frequency (Hz)	Mission				
		SNPP	NOAA-20	J2	J3	J4
1	2.38E+10	-0.00001827	-2E-05	TBD	TBD	TBD
2	3.14E+10	-0.0000056	-1.1E-05	TBD	TBD	TBD
3	5.03E+10	-0.00000345	-3.1E-06	TBD	TBD	TBD
4	5.18E+10	-0.00001561	-1.5E-05	TBD	TBD	TBD
5	5.28E+10	-0.00001495	-1.5E-05	TBD	TBD	TBD
6	5.36E+10	-0.00001956	-2E-05	TBD	TBD	TBD
7	5.44E+10	-0.00001541	-1.5E-05	TBD	TBD	TBD
8	5.49E+10	-0.0000163	-1.5E-05	TBD	TBD	TBD
9	5.55E+10	-0.00000987	-9.3E-06	TBD	TBD	TBD
10	5.73E+10	-0.00001021	-1E-05	TBD	TBD	TBD
11	5.73E+10	-0.00005709	-5.7E-05	TBD	TBD	TBD
12	5.73E+10	-0.00012788	-0.00012	TBD	TBD	TBD
13	5.73E+10	-0.00012447	-0.00012	TBD	TBD	TBD
14	5.73E+10	-0.00012398	-0.00012	TBD	TBD	TBD
15	5.73E+10	-0.00012456	-0.00012	TBD	TBD	TBD
16	8.82E+10	-0.00021966	-0.00023	TBD	TBD	TBD
17	1.66E+11	-0.00037084	-0.00035	TBD	TBD	TBD
18	1.83E+11	-0.0177925	-0.01846	TBD	TBD	TBD
19	1.83E+11	-0.00759156	-0.00762	TBD	TBD	TBD
20	1.83E+11	-0.00320016	-0.00333	TBD	TBD	TBD
21	1.83E+11	-0.00115035	-0.00115	TBD	TBD	TBD
22	1.83E+11	-0.0003709	-0.00035	TBD	TBD	TBD

Table 4. ATMS Band Correction Coefficient c_1

Ch. No.	Center Frequency (Hz)	Mission				
		SNPP	NOAA-20	J2	J3	J4
1	2.38E+10	1.00001087	1.000012	TBD	TBD	TBD
2	3.14E+10	1.00000254	1.000005	TBD	TBD	TBD
3	5.03E+10	1.00000099	1.000001	TBD	TBD	TBD
4	5.18E+10	1.00000436	1.000004	TBD	TBD	TBD
5	5.28E+10	1.0000041	1.000004	TBD	TBD	TBD
6	5.36E+10	1.00000529	1.000005	TBD	TBD	TBD
7	5.44E+10	1.00000411	1.000004	TBD	TBD	TBD
8	5.49E+10	1.0000043	1.000004	TBD	TBD	TBD
9	5.55E+10	1.00000258	1.000002	TBD	TBD	TBD
10	5.73E+10	1.00000259	1.000003	TBD	TBD	TBD
11	5.73E+10	1.00001448	1.000015	TBD	TBD	TBD
12	5.73E+10	1.00003243	1.000031	TBD	TBD	TBD
13	5.73E+10	1.00003156	1.000031	TBD	TBD	TBD
14	5.73E+10	1.00003144	1.000031	TBD	TBD	TBD
15	5.73E+10	1.00003159	1.000032	TBD	TBD	TBD
16	8.82E+10	1.00003698	1.00004	TBD	TBD	TBD
17	1.66E+11	1.00003471	1.000033	TBD	TBD	TBD
18	1.83E+11	1.00140905	1.00146	TBD	TBD	TBD

19	1.83E+11	1.00060682	1.000608	TBD	TBD	TBD
20	1.83E+11	1.00025922	1.000269	TBD	TBD	TBD
21	1.83E+11	1.00009519	1.000093	TBD	TBD	TBD
22	1.83E+11	1.00003163	1.00003	TBD	TBD	TBD

6.3 Effective Blackbody Radiance

The warm load radiance is derived from the radiance determined from the band-corrected warm load brightness temperature, plus a radiance bias correction factor. This correction factor is allowed to depend on the receiver's physical temperature, T_{rx}. The blackbody physical temperature, T, is implemented as a weighted average of warm load PRTs in two dimensions – PRT number and scan number - that allows

a. more weight to be given to certain PRTs than others, and
b. implementation of variable, time-dependent weighting coefficients (i.e., samples closest in time are given larger weights than those further away)

The weighting coefficients are specified in ancillary processing tables that can be changed if necessary. By applying the band correction formula to the blackbody physical temperature, as described in the previous subsection, the warm target band-corrected brightness temperature, T', can be computed.

The warm target radiance bias error is dependent on four terms - warm load emissivity, physical temperature, external radiation, and reflector emission - and can be expressed as follows:

$$\Delta R_w(T_{rx}) = \Delta R_{w,em}(T') + \Delta R_{w,temp}(T') + \Delta R_{w,cp}(T', T_{ex})$$
$$+ \Delta R_{w,reflEmis}\left(\epsilon_{refl}, R(T_{refl}), R_w(T'), \theta\right). \tag{39}$$

The first three terms are discussed below, and the reflector emissivity contribution is discussed in Section 6.5.2.

If the warm target is not a perfect blackbody, the emitted radiation is less than the value computed from the Planck function, resulting in a difference of:

$$\Delta R_{w,em} = (\epsilon - 1) \cdot R_w(T'), \tag{40}$$

where R_w is warm target radiance, and can be calculated from the warm target band-corrected brightness temperature. For ATMS, the requirement for warm target effective emissivity is no less than 0.9999. Thus, at a temperature of 300 K, the resulting bias error in brightness temperature is no more than 0.03 K. The uncertainty of the warm target radiance, $R_{w,temp}$, depends on the temperature drifts, temperature gradients, and inaccurate temperature measurements.

Temperature drift is the target temperature change between the time of radiometric observation and the time that the physical temperature is measured. For ATMS, the maximum time delay is the 2.67 s scan period, and the maximum thermal drift rate is required to be smaller than 0.001 K/s. Thermal analyses indicate that the actual maximum drift rate, which occurs at the eclipse when the angle between sun vector and satellite orbit plane, or beta angle, is about 80°, will be no greater than this requirement. In the actual ATMS design, the physical temperature measurements are centered at the same time as the warm calibration radiometric measurements. Therefore, for the nominal case bias error budget, this item is reduced to a negligible contribution [NG, 2017].

The warm load target temperature spatial gradients calculated from target PRT measurements for S-NPP, NOAA-20, J02 and J03 ATMS, computed from pre-launch thermal vacuum data, are 0.02

K, 0.05 K, 0.14 K and 0.2 K, respectively. The use of multiple temperature sensors distributed throughout the warm load allows for averaging that reduces horizontal gradients. However, the vertical gradients still exist and will contribute directly to the calibration bias error. The vertical gradients are a function of the horizontal position on the pyramidal tines, and the effect of this on calibration bias error will be the temperature error averaged over the horizontal plane. The temperature measurement accuracy pertains to the accuracy of the PRT sensors and their associated read-out electronics. The single four-wire PRT accuracy is about 0.10 K. The average of readings from seven PRTs, which is the minimum required for each calibration target, will reduce the bias error. The reduction factor though is largely unknown since some of the error terms may be partially correlated. The resulting end-of-life (EOL) value for a single PRT is therefore used for the bias error budget study.

In Equation (38), the external radiation term, $R_{w,cp}$ is caused by the imperfect coupling of the reflector/shroud assembly to the warm load. The error due to this coupling is given by:

$$\Delta R_{w,cp} = C_g \cdot (R_w - R_{ex}), \tag{41}$$

where C_g is the coupling factor, and R_w and R_{ex} are the radiance of warm load and external environment, respectively. The worst-case condition is when the warm load is heated to a maximum and the external environment is at a minimum. Thermal analyses indicate that the maximum target temperature is 330 K. As illustrated in Figure 12, the environment, facing the Earth, with reflective obstructions on all sides, is approximated as about a 75% view of Earth and 25% view of cold space. At a minimum Earth brightness temperature of 150 K, this gives a radiance error in terms of brightness temperature of 0.2 K.

Considering the target emissivity error and coupling loss, the warm load target bias for on-orbit calibration can be calculated as:

$$\Delta R_w = -R(T' = 282K) \cdot (1 - \epsilon) - C_g \cdot \left(R_w(T') - R_{ex}(T_{ex} = 113.3K)\right) \tag{42}$$
$$+ \Delta R_{w,reflEmis}\left(\epsilon_{refl}, R(T_{refl}), R_w(T'), \theta\right),$$

where R_w is warm load target radiance and R_{ex} is radiance of the external environment. In operational calibration algorithm, a brightness temperature of 113.3K was used to calculate the R_{ex}. The warm load target emissivity and coupling factor for each of 22 channels of SNPP and NOAA-20 ATMS can be found in the instrument calibration data book.

6.4 Effective Space Radiance

A value of 2.728 K is used for the cosmic background temperature, T_c, which can be transformed into radiance through Planck's equation. Uncertainties in the radiance of the cold target observation are dependent upon the Earth contamination through antenna sidelobes, $\Delta R_{c,se}$, the near-field spacecraft and instrument blockage, $\Delta R_{c,sc}$, the uncertainty of the actual cosmic radiation, $\Delta R_{c,cosmic}$, and the antenna reflector emission, $\Delta R_{c,reflEmis}$ - i.e.,

$$\Delta R_c = \Delta R_{c,se} + \Delta R_{c,sc} + \Delta R_{c,cosmic} + \Delta R_{c,reflEmis}. \tag{43}$$

The first three terms are discussed below, but the reflector emissivity contribution is discussed in Section 6.5.2.

The magnitude of the Earth radiation contamination can be either predetermined from ground-measured antenna patterns or calculated from cold space observations collected during the ATMS instrument post-launch roll maneuver. The estimate computed using the antenna pattern involves

integration of a worst-case ATMS far-field antenna pattern over the angular region subtended by the Earth for the primary cold calibration beam position at a spacecraft altitude of 833 km. Both co- and cross-polarized antenna patterns were employed in the computations, because the rotation of the reflector with respect to the feedhorn causes a rotation of the incident vertical and horizontal polarization vector with respect to the feedhorn wave guide slot. For Suomi NPP and NOAA-20 ATMS, the worse-case cold target calibration error is about 0.3 K to 0.5 K from Earth contamination.

The estimate of cold-target radiance uncertainty related to the near-field spacecraft and instrument blockage involves an integration of the near-field energy density of the antenna over regions of the spacecraft structures. The goal of this step is to determine the fraction of energy received from spacecraft reflections of Earth radiation. This was done both for the cases of maximally allowed spacecraft intrusions into the cold space hemisphere, and for an expected typical case based on proposed satellite configurations. For Suomi NPP and NOAA-20 ATMS, the worse-case cold target calibration error is about 0.08 K to 0.13 K from the spacecraft contamination.

Finally, the uncertainty in computing the cosmic background radiance is determined by the cosmic temperature, which is 2.72548 ± 0.00057 K, and can be transformed easily into radiance space. This term of Equation (42) is found to be negligible.

The Earth and spacecraft radiance interception percentage with respect to total incoming radiance, which determines cold target radiance uncertainty, can be found in the ATMS calibration data book. Biases are calculated by assuming brightness temperature of 290K for the Earth and for reflected radiation from the spacecraft. The value of the SDR algorithm correction is half of the sum of the Earth and spacecraft predicted maximum contributions.

<u>Lunar Intrusion Correction</u>

Nominally, the ATMS cold space view position is chosen from the four possible space view positions to provide the least space view radiance contamination. There are instances though when the Moon enters into the specified ATMS space view and contaminates the signal. In ATMS operational TDR datasets, lunar intrusion (LI) is identified by the quality flag defined as "Moon in Space View." The definition of a LI event is when the Moon disk enters the ATMS antenna main beam during a space view. After the launch of Suomi-NPP and NOAA-20 satellites, it was observed that LI events happened several times a year and would affect several consecutive orbits. Since the lunar surface brightness temperature can vary from 120 K to 380 K, and is much higher than the 2.7 K cosmic background temperature used in calibration, lunar radiation can seriously impact calibration accuracy if it is not corrected. For most of the current space-borne microwave radiometers operating in polar orbit at an altitude around 800km above the Earth's surface, the apparent angle subtended by the disk of the Moon is about 0.5°, which is much smaller than beam width of the ATMS observations. The method to determine the radiance contamination related to the Moon in space view, described in Yang and Weng (2016), is briefly described below.

When the Moon appears in the satellite observation field of view (FOV), the effective microwave brightness temperature of the Moon disk, TB_{moon}^{ref}, is a function of the ATMS antenna response function, G_{ant}, as well as the Moon disk normalized solid angle, Ω_{moon}, and average lunar brightness temperature, TB_{moon}^{disk}. This is given below as follows:

$$TB_{moon}^{ref} = \Omega_{moon} \cdot G_{ant} \cdot TB_{moon}^{disk} \, . \tag{44}$$

Assuming the azimuthal asymmetry is insignificant, the antenna response within the mean beam range can then be accurately simulated by the following one-dimension Gaussian function:

$$G_{ant}(\alpha) = e^{\frac{(\alpha - \alpha_0)^2}{2\sigma^2}} ,$$

(45)

where α is the separation angle between the antenna boresight and Moon-in-Spaceview vector, α_0, is the beam pointing error, and σ is an antenna parameter that is a function of the angle defining the 3-dB beam width θ_{3db} – i.e., $\sigma = 0.5\ \theta_{3dB}/\sqrt{2log2}$. The normalized solid angle of the moon, Ω_{moon}, is calculated as a solid angle of the moon disk normalized by the antenna beam solid angle, Ω_A, with the following expression:

$$\Omega_{moon} = \frac{\pi \left(\frac{r_{moon}}{D_{moon}}\right)^2}{\Omega_A} .$$

(46)

In this expression, r_{moon} and D_{moon} are the radius and diameter of the Moon, respectively. Also, Ω_A can be given as $\Omega_A = \iint_{4\pi} G(\theta, \phi) sin\theta d\theta d\phi$. In this expression, θ and ϕ are the antenna elevation and azimuth angles, respectively. For ATMS calibration, antenna-related parameters σ and Ω_A were calculated from ground measurements of antenna pattern, and α_0 is derived from large samples of lunar observations by using an optimized regression algorithm. In Equation (43), the average brightness temperature of the Moon's disk is a function of Moon phase angle, Θ, and can be calculated from the equation below as

$$TB_{moon}^{disk} = 95.21 + 104.63 \cdot (1 - cos\Theta) + 11.62$$
$$\cdot (1 + cos2\Theta) .$$

(47)

It should be noted that the above experimental expression for TB_{moon}^{disk} is derived under an assumption that the average emissivity of lunar surface is about 0.95, and there is no frequency dependence of brightness temperature of the Moon.

For each of the four cold space view readings, if ΔT_c is larger than a threshold of 0.2 K, this cold space view reading is flagged as being contaminated by lunar intrusion and excluded in the SDR calibration. It needs to be pointed out that ΔT_c is only used for detecting the contaminated cold space view reading, not used to correct it.

Cold space view readings that are not contaminated by lunar intrusion (e.g., up to four readings) are used in the calibration processing. However, there is high probability that all four readings are contaminated in a single scan line, particularly for the channels with a 5.2° FOV. To avoid data gaps (could be up to 200 scans), cold space view readings least effected by lunar intrusion are selected for calibration, with additional lunar radiation terms calculated from Eq (31) included in cold end calibration radiance.

6.5 Antenna Temperature

As mentioned in Section 5. In-flight Calibration System, the approach adopted for ATMS is to first use the linear approximation to estimate radiance, R_{lin}, and then estimate and apply radiance corrections, ΔR, to this linear retrieved radiance. The radiance corrections include a radiance correction for the non-linearity of the calibration curves, ΔR_{nl}, as well as a radiance correction for the antenna reflector emission, $\Delta R_{s,reflEmis}$. This combined correction to can be simply expressed as:

$$\Delta R = \Delta R_{nl} + \Delta R_{s,reflEmis} \, . \tag{48}$$

Once the radiance corrections have been added to the linear radiance estimate, an antenna radiance is established. This can be converted to ATMS TDR product brightness temperature in units of K, by converting corrected radiance to brightness temperature using Plank's Function. In the two subsections below, more details about the radiance corrections are provided.

6.5.1 On-Orbit Non-linearity Correction

The nonlinearity parameter, Q, in Equation (15) can be expressed as a function of the nonlinearity parameter, μ, as follows:

$$\Delta R_{nl} = \mu \cdot (\overline{R_w} - R_c)^2 \cdot x \cdot (x - 1) \, , \tag{49}$$

where R_w and R_c are the radiance of warm and cold calibration targets, and x is the normalized scene counts with $x = (C_s - C_c)/(C_w - C_c)$. The values of μ can be obtained from ATMS thermal vacuum (TVAC) measurement data acquired within the scene temperature range of 83 K to 330 K for Suomi-NPP, and 93 K to 330 K for NOAA-20 ATMS. However, for ATMS on-orbit calibration, the cold calibration temperature is approximately 3 K. Thus, the nonlinearity value must be estimated by extrapolating TVAC data down to 3 K. By using Equation (48) above, one can compute the nonlinearity term for all scene temperatures within and beyond the range defined by the 83 K or 93 K minimum value, and the 330 K maximum. Since the nonlinearity parameter μ is sensitive to receiver temperature, T_{rx}, the μ parameter needs to be derived for different receiver temperature settings. For ATMS TVAC testing, the μ parameters are derived for receiver temperature settings of -10°C, 5°C, and 20°C, in order to cover the possible on-orbit operational receiver temperature variation range. Then a quadratic fitting function can be used define the relationship between T_{rx} and μ as given below:

$$\mu = a_0 \cdot T_{rx}^2 + a_1 \cdot T_{rx} + a_2 \, . \tag{50}$$

Note, that the nonlinearity term Q in Equation (15) can also be expressed as a function of maximum nonlinearity, R_{nlmax}, as $\Delta R_{nl} = R_{nlmax} \cdot [4 \cdot (x - 0.5)^2 - 1]$, where $R_{nlmax} = \mu \cdot (\overline{R_w} - R_c)^2/4$

6.5.2 Reflector Emission Correction

Equation (30) provides a physical model for simulating receiver response to incoming unpolarized radiation obtained through a non-lossless polarizing scan antenna reflector. This relates to the case of cold space scans taken during the satellite pitch-over maneuver. When a non-lossless plane reflector is used to scan the scene, uniform unpolarized radiation can be polarized and quantified as a function of antenna reflectivity, reflector radiance, scene radiance, and scan angle. For QV channels, the relationship between brightness temperature and scan angle is a sine-squared curve, and for QH channels it follows a cosine-squared curve. The impact of reflector thermal radiation can become significant for the cosmic background scene temperature of 2.73 K, which is the case for the cold space view portion of the ATMS scan cycle. For example, if the reflector reflectivity is only 0.994, then using the assumed cold target brightness temperature of 2.73 K in calibration can have an error of about 2 K. At this reflector reflectivity, a value for the cold space view of about 4.5 K may be appropriate, and should be considered.

From the theory described in Yang et. al. (2016), the antenna emissivity, ϵ_h, at 45° angle with respect to the scattering plane can be solved with the following equation:

$$\epsilon_h$$
$$= \frac{\delta \cdot (\overline{R_w} - R_c)}{\delta \cdot \left[(\overline{R_w} - R_{rfl}) \cdot sin^2\theta_w - (R_c - R_{rfl}) \cdot sin^2\theta_c\right] - (R_c - R_{rfl}) \cdot (sin^2\theta_s - sin^2\theta_c)} \quad (51)$$

In equation above, $\overline{R_w}$, R_c, and R_{rfl} represents the warm load, cold space view and antenna reflector radiance, respectively. Meanwhile, the parameters θ_w, θ_c, and θ_s respectively represent the scan angle associated with the warm load, space view, and scene. Finally, $\delta = (C_s - \overline{C_c})/(\overline{C_w} - \overline{C_c})$ is the normalize scene counts. The channel dependent flat reflector emissivities of Suomi-NPP and NOAA-20 ATMS are derived from pitch observations by using Equation (50), and are listed in Table 5.

Table 5. NOAA-20/S-NPP ATMS Reflector Emissivity

Channel	NOAA-20 ATMS Reflector Emissivity	SNPP ATMS Reflector Emissivity
1	0.0018	0.0025
2	0.0014	0.0026
3	0.0004	0.0021
4	0.0004	0.0022
5	0.0005	0.0021
6	0.0004	0.0023
7	0.0006	0.0023
8	0.0003	0.0024
9	0.0004	0.0023
10	0.0007	0.0025
11	0.0006	0.0024
12	0.0007	0.0026
13	0.0007	0.0028
14	0.0003	0.0022
15	0.0003	0.0026
16	0.0017	0.0046
17	0.0004	0.0029
18	0.0006	0.0039
19	0.0004	0.0039
20	0.0002	0.0039
21	0.0006	0.0039
22	0.0006	0.0036

For on-orbit calibration, the cold space view and warm load radiance are corrected for reflector emission by using the equation below:
For Q_v channels

$$\Delta R_{x,reflEmis} = \epsilon_h \cdot \left(R_{rfl} - R_x\right) + \left(R_{rfl} - R_x\right) \cdot \left(\epsilon_v - \epsilon_h\right) \qquad (52)$$
$$\cdot \sin^2\theta \,.$$

For Q_h channels

$$\Delta R_{x,reflEmis} = \epsilon_h \cdot \left(R_{rfl} - R_x\right) + \left(R_{rfl} - R_x\right) \cdot \left(\epsilon_v - \epsilon_h\right) \cdot \cos^2\theta \,. \qquad (53)$$

In the equation above, x can be c, w, or s, which represent cold space, average warm load or earth scene respectively. The reflector emission correction equations for antenna temperature at each of the FOV positions is given below:

$$T_a' = C_0 + C_1 \cdot T_a \,. \qquad (54)$$

In the equation above, C_0 and C_1 are correction coefficients and can be calculated from reflector emissivity and reflector temperature as below:

For Q_v channels

$$C_0 = \frac{-T_{rfl} \cdot \epsilon \cdot \left(1 + (1 - \epsilon)\right)sin^2\theta}{(1 - \epsilon) \cdot (1 - \epsilon sin^2\theta)} \qquad (55)$$

$$C_1 = \frac{1}{(1 - \epsilon) \cdot (1 - \epsilon sin^2\theta)} \qquad (56)$$

For Q_h channels

$$C_0 = \frac{-T_{rfl} \cdot \epsilon \cdot \left(1 + (1 - \epsilon)\right)cos^2\theta}{(1 - \epsilon) \cdot (1 - \epsilon cos^2\theta)} \qquad (57)$$

$$C_1 = \frac{1}{(1 - \epsilon) \cdot (1 - \epsilon cos^2\theta)} \,. \qquad (58)$$

6.6 Data Quality Control

The SDR code examined for the first version of this document contains only rudimentary data quality control (QC) and quality assessment (QA). Subsequent algorithm updates have incorporated additional quality checking process [NASA, 2017].

PRT Quality Checks:

1) PRT quality check – limits

The converted warm load PRT temperatures are checked against predetermined gross limits. Those falling outside the limits are considered "bad":

$$T_i < T_{low} \text{ or } T_i > T_{upp} \rightarrow \text{"bad-}T_i\text{"}$$

2) PRT quality check – self-consistency

The PRT temperatures are then checked for self-consistency (i.e., data fluctuation). This is done by comparing all temperatures not flagged as bad with each other. Any PRT's temperature that differs by more than a fixed limit from at least two other PRTs readings will be flagged as "bad":

$$|T_i - T_j| > \Delta T_{max} \text{ and } |T_i - T_n| > \Delta T_{max} \rightarrow \text{"bad-}T_i\text{"}$$

The number of "good" PRTs is then checked. If there are less than five "good" PRTs for the KAV target or four for the WG target, all PRTs within that group will be flagged as "bad". These numbers can be adjusted in the ancillary parameter file. "Bad" PRTs are excluded from the calibration process.

3) PRT quality check – data sufficiency

If the weight-sum of "good" PRT readings used in the multi-scans averaging falls below a specified percentage, it is deemed not possible to reliably determine the warm load temperature for the current calibration cycle:

$$(\textstyle\sum_i W_i)/W_{total} < W_{threshold\_prt} \rightarrow \text{“bad-}\overline{T_W}\text{”}$$

Failing the data sufficiency test will result in an unsuccessful calibration cycle.

Warm Count Quality Checks:

1)   Quality check – limits

Each count from each channel is checked against pre-defined channel-specific gross limits. Those fall outside the limits are flagged as "bad":

$$Cw_i < Cw_{low} \text{ or } Cw_i > Cw_{upp} \rightarrow \text{“bad-}Cw_i\text{”}$$

2)   Quality check – self consistency

The counts are checked for self-consistency. Each count not flagged as "bad" is compared with other counts in the same scan. Any count that differs by more than a fixed limit from at least two other counts will be flagged as "bad":

$$|Cw_i - Cw_j| > \Delta Cw_{max} \text{ and } |Cw_i - Cw_k| > \Delta Cw_{max} \rightarrow \text{“bad-}Cw_i\text{”}$$

The number of "good" samples is then checked. If there are less than three "good" samples, this scan will be flagged as "bad" and not included in the multi-scans averaging.

3)   Quality check – gain error

If the lowest "good" warm count is smaller than or equal to the highest "good" cold count, all the warm counts and cold counts from this scan will be flagged as "bad" and not included in the multi-scans averaging.

4)   Quality check – data sufficiency

If the weight-sum of all "good" scans falls below a specified percentage, it is deemed impossible to reliably determine the averaged warm count for the current calibration cycle. Failing the data sufficiency test will result in an unsuccessful calibration cycle.

Cold Count Quality Checks:

The cold count quality checks are identical to the warm count checks, with limits appropriate for the cold counts.

All the limits and thresholds would be set initially during pre-launch to allow all data to pass through. After launch, these numbers shall be adjusted accordingly based on operational experiences.

7. TDR to SDR Conversion

As a cross-track scanning microwave radiometer, pure vertical (V) or horizontal (H) polarization measurements of ATMS only occur at the nadir direction. At other scan angles, the measurements represent a mixed contribution from both V and H polarizations. Thus, it is necessary to define the quasi-vertical and quasi-horizontal antenna brightness temperatures (TDR), T_a^{Qv} and T_a^{Qh}, which are defined as,

$$T_a^{Qv} = T_a^v \cos^2 \theta + T_a^h \sin^2 \theta \tag{59}$$

$$T_a^{Qh} = T_a^v \sin^2 \theta + T_a^h \cos^2 \theta \tag{60}$$

where T_a^v and T_a^h are the antenna brightness temperatures of the vertically polarized and horizontally polarized components, respectively, following the conventional definition. The variable θ is the scan angle from nadir. This is an approximation derived from the general Stokes vector transformation with an assumption of zero third and fourth Stokes components. Thus, the ATMS antenna receives a linear combination of the pure vertical and horizontal components.

For a microwave antenna system, the radiative components from the Earth and other targets are collected through its main beam and the side lobes. The magnitude of side lobes depends on both frequency and antenna size. In general, the higher the frequency and the larger the antenna size, the narrower the main beam and the smaller the side-lobe effect. Based on the normalized antenna pattern, the main beam width, and co- and cross-polarized main beam efficiencies, are computed. Note that the main beam efficiency is defined using the half-power point. Similarly, the normalized antenna pattern is also used to determine the co- and cross-polarized efficiencies of the side lobes. The main beam efficiency of ATMS antenna are higher than 95% at all three scan positions, while the maximum magnitude of either of the side lobes is less than -30dB. The satellite measured radiation represents a convolution of not only the main beam efficiency of detected Earth radiance, but also the side lobe contributions from radiance emanating from the Earth, cold space and the satellite platform. This is described by the following equation:

$$T_a^{Qp} = \int_{\Omega_{ME}} d\Omega \cdot \left(G_{pp} \cdot T_{Qp} + G_{pq} \cdot T_{Qq}\right) + \int_{\Omega_{SE}} d\Omega \cdot \left(G_{pp} \cdot T_{Ep} + G_{pq} \cdot T_{Eq}\right)$$
$$+ \int_{\Omega_{SC}} d\Omega \cdot \left(G_{pp} + G_{pq}\right) \cdot T_C \tag{61}$$

In this equation, the subscript Qp can represent either the Qv or Qh polarization direction, and Qq is the polarization direction perpendicular to Qp. For example, if $Qp = Qv$, then $Qq = Qh$. The other parameters can be described as follows: G_{pp} and G_{pq} are the normalized antenna gain in the far-field - i.e., Earth and cold space - for co- and cross-polarization, respectively; T_{Qp} and T_{Qq} are the brightness temperatures associated with the Earth scene radiance intercepted by the antenna main beam in each polarization direction; T_{Ep} and T_{Eq} are similar Earth brightness temperatures for the side lobe region, T_C is the cosmic background radiation brightness temperature. The two variables Ω_{ME} and Ω_{SE} are respectively the solid angles of the antenna main beam and side lobes that intersect with the Earth, while Ω_{SC} is the solid angle of the side lobes sensing cold space. The first term in the equation is the earth radiation entering into the receiver system through the antenna main beam, which is determined by the -3dB beam width; the second term is the radiation sensed through the side lobes that is out of the main beam but within the earth view sector; and the third term is the cold space radiation sensed through the side lobes. Note that the term that would capture the contribution to antenna temperature from the satellite platform has been neglected.

The antenna pattern $G(\theta, \phi)$ used in the ATMS antenna pattern correction (APC) is generated as a combination of an analytical antenna pattern generated by the GRASP model and that created from vendor laboratory measurements. This approach reduces the artificial effects in the far side lobe regions where the normalized antenna gain is below -60dB. These hybrid antenna datasets are generated in the polar coordinate system at a 0.01° resolution in the elevation (θ) coordinate and at the following four azimuth angles: $\phi = 0°$; $\phi = 45°$; $\phi = 90°$; and $\phi = 135°$. To calculate the APC coefficients at each scan angle, the antenna pattern is first interpolated to a 0° to 360° azimuth angle range, and then projected to the antenna coordinate system at each scan angle, α, by using equation below:

$$G(\alpha) = R_{ant/pol} \times G(\theta, \phi), \qquad (62)$$

where $R_{ant/pol}$ is rotation matrix given by equation below:

$$R_{ant/pol} = \begin{bmatrix} 1 & 0 & 0 \\ 0 & cos(\alpha) & sin(\alpha) \\ 0 & -sin(\alpha) & cos(\alpha) \end{bmatrix}. \qquad (63)$$

The first two terms in Equation (60) can be combined by applying the assumptions that Earth scene radiation is unpolarized, and that Earth scene brightness temperatures are homogeneous within the Earth main beam and side lobe solid angle regions. This leads to an antenna pattern corrected scene brightness temperature that can be written as:

$$Tb = \frac{Ta - \eta_c \cdot T_C}{\eta^{pp} + n^{pq}}. \qquad (64)$$

These assumptions are reasonable for sounding channels, at which unpolarized Earth scene radiation is being collected. But they will introduce errors for window channels, especially for those Earth scenes that contain predominantly clear-sky ocean surface, where the polarization of incoming radiation cannot be ignored. In equation above, parameters η^{pp}, η^{pq}, and η^c are the Earth scene co-polarization coefficient, Earth scene cross-polarization coefficient, and the cold space spill over combined co- and cross-polarization coefficients, respectively. They are defined as follows:

$$\eta^{pp} = \frac{\int_{\Omega_{ME+SE}} G_{pp}(\theta, \phi) d\theta d\phi}{G_{total}}, \qquad (65)$$

$$\eta^{pq} = \frac{\int_{\Omega_{ME+SE}} G_{pq}(\theta, \phi) d\theta d\phi}{G_{total}}, \text{ and} \qquad (66)$$

$$\eta^c = \frac{\int_{\Omega_C} \left(G_{pp}(\theta, \phi) + G_{pq}(\theta, \phi) \right) d\theta d\phi}{G_{total}}. \qquad (67)$$

where G_{total} is defined as the far-field antenna pattern integrated over areas that are clear of satellite and instrument blockage: $G_{total} = \int_{\Omega_{ME+SE+C}} \left(G_{pp}(\theta, \phi) + G_{pq}(\theta, \phi) \right) d\theta d\phi$.

The correction coefficients can be directly calculated from antenna pattern data by using Equations (64), (65), and (66), if the integration boundary is known for each equation. The antenna angles subtended by the Earth and satellite platform can be calculated from RF pattern analysis during

prelaunch test. During NOAA-20 post-launch on-orbit testing, a special ATMS instrument scan operation was used in which 148 samples were collected over the entire 360° scan angle at a scan rate of 0.135 deg/ms. The interception angles at inflection points related to the Earth and satellite/instrument boundaries were determined more accurately than ground test, and are used in Equations (64), (65), and (66).

Equation (63) was derived under the assumption that the incoming radiation is mainly concentrated in the main beam, and brightness temperatures within the solid angle covering the
Earth region is homogeneous. For low-frequency channels of ATMS with 5.2° and 2.2° beam width, the inhomogeneity will become non-negligible. This is especially true at the scan edge when the size of the FOV is much larger. To accommodate the impacts of FOV brightness temperature inhomogeneity, the antenna gain was projected onto the Earth surface following the regular geolocation process with a resolution of 0.01° in elevation angle and 1° in azimuth angle. The antenna temperature at each beam position then can be calculated by convolving the antenna pattern and scene brightness temperature from equation below:

$$T_a^{Qp} = \int_{\Omega_E} G_{pp}(\theta, \phi) \cdot T_{Qp}(\theta, \phi) d\theta d\phi + \int_{\Omega_E} G_{pq}(\theta, \phi) \cdot T_{Qq}(\theta, \phi) \, d\theta d\phi + \eta^C \cdot T_C . \tag{68}$$

The co-polarization coefficients in Equation (64) then can be corrected by using the equation below:

$$\eta^{pp}(\alpha) = \frac{T_a^{Qp}(\alpha) - \eta^{pq} \cdot T^{Qq}(\theta = 0°, \phi = 0°) - \eta^C \cdot T_C}{T^{Qp}(\theta = 0°, \phi = 0°)} . \tag{69}$$

8. References

Anderson, K., 2004: ATMS SDR Algorithm Description; NGES TM-01-380D

Hersman, M. S., & Poe, G. A. (1981). Sensitivity of the total power radiometer with periodic absolute calibration. IEEE Transactions on Microwave Theory and Techniques, 29(1), 32–40.

Kim, E., C.-H. J. Lyu, K. Anderson, R. Vincent Leslie, and W. J. Blackwell (2014), S-NPP ATMS instrument prelaunch and on-orbit performance evaluation, *Journal of Geophysical Research: Atmospheres*, *119*(9), 5653-5670, doi:10.1002/2013jd020483.

Mo, T., 2002: Calibration of the Advanced Microwave Sounding Unit-A Radiometers for NOAA-N and NOAA-N', NOAA Technical Report NESDIS 106, 55 pp.

Mo, T. and K. Jarva, "Microwave Humidity Sounder Calibration Algorithm," NOAA Technical Report NESDIS 116, 22 pp.

NASA (2017), Joint Polar Satellite System (JPSS) Operational Algorithm Description (OAD) Document for Advanced Technology Microwave Sounder (ATMS) Sensor Data Record (SDR) Software, Tech. Rep., NASA/Goddar Space Flight Center, Greenbelt, Maryland, US

NG (2017), Joint Polar Satellite System (JPSS) Advanced Technology Microwave Sounder (ATMS) Calibration Data Book JPSS1 ATMS P/N 1362460-1, S/N 303, Tech. Rep., Northrop Grumman, Azusa, California 91702, US.

NGES (2012), Advanced Technology Microwave Sounder (ATMS) Calibration Data Book ATMS PFM P/N 1362460-1 S/N 302, *Tech. Rep.*, Northrop Grumman, Electronic Systems, Azusa, California 91702, US.

Poe, G. A., 1990: Optimum Interpolation of Imaging Microwave Radiometer Data, *IEEE Trans. Geosci. Remote Sens.*, 28, 800-810

Tian, M., X. Zou, and F. Weng (2015), Use of Allan Deviation for Characterizing Satellite Microwave Sounder Noise Equivalent Differential Temperature (NEDT), *IEEE Geoscience and Remote Sensing Letters*, *12*(12), 2477-2480, doi:10.1109/lgrs.2015.2485945.

Weng, F., X. Zou, N. Sun, H. Yang, M. Tian, W.J. Blackwell, X. Wang, L. Lin, and K. Anderson, 2013: Calibration of Suomi National Polar-Orbiting Partnership (NPP) Advanced Technology Microwave Sounder (ATMS), *J. Geophys. Res. Atmos.,* **118**, 1–14, doi:10.1002/jgrd.50840

Weng, F., H. Yang, and X. Zou, 2012: On Convertibility from Antenna to Sensor Brightness Temperature for Advanced Technology Microwave Sounder (ATMS*), IEEE Geosci. Remote. Sens. Letter,* 10.1109/LGRS.2012.2223193

Weng, F. and X. Zou, 2013: Errors from Rayleigh–Jeans Approximation in Satellite Microwave Radiometer Calibration System, *Appl. Optics*, 12, 505-508.

Weng, F. and H. Yang, 2016: Validation of ATMS calibration accuracy using Suomi NPP pitch

maneuver observations. *Remote Sensing*, 8(4), 332.

Yang, H., and F. Weng, 2016: On-Orbit ATMS Lunar Contamination Corrections, *IEEE Transactions on Geoscience and Remote Sensing*, Vol. 54 Issue: 4, 1-7.

Yang, H., F. Weng, and K. Anderson, 2016: Estimation of ATMS Antenna Emission from Cold Space Observations, *IEEE Geoscience and Remote Sensing*, 10.1109/TGRS.2016.2542526.